



**HAL**  
open science

## Top-down Surfactant-Free Synthesis of Supported Palladium-Nanostructured Catalysts

Christian Schott, Peter Schneider, Kais Sadraoui, Kun-ting Song, Batyr Garlyyev, Sebastian Watzele, Jan Michalička, Jan Macak, Arnaud Viola, Frédéric Maillard, et al.

► **To cite this version:**

Christian Schott, Peter Schneider, Kais Sadraoui, Kun-ting Song, Batyr Garlyyev, et al.. Top-down Surfactant-Free Synthesis of Supported Palladium-Nanostructured Catalysts. *Small Science*, 2024, 4 (3), 10.1002/smssc.202300241 . hal-04395364

**HAL Id: hal-04395364**

**<https://hal.science/hal-04395364>**

Submitted on 15 Jan 2024

**HAL** is a multi-disciplinary open access archive for the deposit and dissemination of scientific research documents, whether they are published or not. The documents may come from teaching and research institutions in France or abroad, or from public or private research centers.

L'archive ouverte pluridisciplinaire **HAL**, est destinée au dépôt et à la diffusion de documents scientifiques de niveau recherche, publiés ou non, émanant des établissements d'enseignement et de recherche français ou étrangers, des laboratoires publics ou privés.

**Top-Down Surfactant-Free Synthesis of Supported Palladium Nanostructured Catalysts**

*Christian M. Schott, Peter M. Schneider, Kais Sadraoui, Kun-Ting Song, Batyr Garlyyev, Sebastian A. Watzele, Jan Michalička, Jan M. Macak, Arnaud Viola, Frédéric Maillard, Anatoliy Senyshyn, Johannes A. Fischer, Aliaksandr S. Bandarenka\*, Elena L. Gubanova\**

C. M. Schott, P. M. Schneider, K. Sadraoui, K.-T. Song, B. Garlyyev, S. A. Watzele  
Physics of Energy Conversion and Storage, Technical University of Munich, James Franck  
Str. 1, 85748 Garching, Germany

Jan Michalička, Jan M. Macak  
Central European Institute of Technology, Brno University of Technology, Purkynova 123,  
61200 Brno, Czech Republic

Jan M. Macak  
Center of Materials and Nanotechnologies, University of Pardubice, Nam. Cs. Legii 565,  
53002 Pardubice, Czech Republic

Arnaud Viola, Frédéric Maillard  
Univ. Grenoble Alpes, Univ. Savoie Mont Blanc, CNRS, Grenoble INP<sup>+</sup>, LEPMI, 38000  
Grenoble, France, <sup>+</sup>Institute of Engineering and Management Univ. Grenoble Alpes

Anatoliy Senyshyn  
Heinz Maier-Leibnitz-Zentrum (MLZ) TUM, Lichtenbergstr. 1, 85748 Garching, Germany

Johannes A. Fischer  
Physics of Energy Conversion and Storage, Technical University of Munich, James Franck  
Str. 1, 85748 Garching, Germany  
E-mail: ge42bap@mytum.de

Aliaksandr S. Bandarenka

Physics of Energy Conversion and Storage, Technical University of Munich, James Franck  
Str. 1, 85748 Garching, Germany

E-mail: [bandarenka@ph.tum.de](mailto:bandarenka@ph.tum.de)

Aliaksandr S. Bandarenka

Catalysis Research Center TUM, Ernst-Otto-Fischer-Str. 1, 85748 Garching, Germany

E-mail: [bandarenka@ph.tum.de](mailto:bandarenka@ph.tum.de)

Elena L. Gubanova

Physics of Energy Conversion and Storage, Technical University of Munich, James Franck  
Str. 1, 85748 Garching, Germany

E-mail: [elena.gubanova@tum.de](mailto:elena.gubanova@tum.de)

Keywords: electrochemical erosion, hydrogen embrittlement, hydrogen evolution reaction,  
nanoparticles, palladium.

Nanostructured palladium (Pd) is a universal catalyst that is widely used in applications ranging from catalytic converters of combustion engine cars to hydrogenation catalysts in industrial processes. Standard protocols for synthesizing such nanoparticles typically use bottom-up approaches. They utilize special and often expensive physical techniques or wet-chemical methods requiring organic surfactants. These surfactants should often be removed before catalytic applications. This manuscript reports the synthesis of Pd nanoparticles (NPs) immobilized on carbon support by electrochemical erosion without using any surfactants or toxic materials. The Pd NPs synthesis essentially relies on a Pd bulk pretreatment, which causes material embrittlement and allows the erosion process to evolve more efficiently, producing homogeneously distributed nanoparticles on the support. The particle formation process depends on the synthesis parameters, such as electrolyte concentration and applied frequency of the sinusoidal signal. Moreover, the synthesized catalyst was tested for hydrogen evolution reaction (HER). The activity evaluations identified optimal synthesis parameters related to the erosion procedure. The electrocatalytic properties of the Pd NPs produced with sizes down to  $6.4\pm 2.9$  nm were compared with a commercially available Pd/C catalyst. The synthesized catalyst outperforms the commercial catalyst within all properties, like specific surface area (SSA), geometric activity (GA), mass activity (MA), specific activity (SA) and durability.

## 1. Introduction

Palladium (Pd) serves as a universal catalyst for electrochemical and non-electrochemical reactions. For instance, it catalyzes the functionalization of propene<sup>[1,2]</sup> with high industrial relevance and the direct oxidation of methane.<sup>[3]</sup> Alternatively, Pd electrochemically generates hydrogen peroxide,<sup>[4]</sup> accessing a highly relevant oxidizing agent in organic synthesis. Aside from fuel generation, Pd and Pd-based alloys compete with state-of-the-art catalysts in direct liquid-fed fuel cells (DLFFCs) and proton-exchange membrane fuel cells (PEMFCs) for fuel consumption reactions.<sup>[5,6]</sup> The former fuel cell system relies on the oxidation reaction of small organic molecules like methanol,<sup>[7,8]</sup> ethanol,<sup>[9]</sup> and formic acid.<sup>[10]</sup> The latter involves the hydrogen oxidation reaction (HOR) and oxygen reduction reaction (ORR).<sup>[11, 12, 13]</sup> Independently of the catalyzed reaction, the efficiency of the Pd catalyst strongly depends on the shape and size of the nanoparticles (NPs). Synthesis methods fabricate and homogeneously disperse NPs on a suitable support material via physical, biological, or chemical mechanisms.<sup>[14]</sup> Among them, surfactant-free methods attract attention since these organic additives contaminate the metallic NP surface and thus decrease the catalytic performance.<sup>[15,16]</sup> To avoid this loss of activity, we present a surfactant-free, cheap, and upscalable top-down electrochemical method, which we call electrochemical erosion, in the scope of our work. The technique applies an alternating potential to metal wires, generating NPs at the metal surface of the wires immersed in an electrolyte suspension. The groups of Hersbach and Koper showed that the electrolyte, especially the involved cation, plays a crucial role in NP formations.<sup>[17]</sup> Especially alkali-metal (AM)-comprised electrolytes (AMOH, where AM = Li, Na, K, and Cs) showed promising results, but NPs formation also occurred for Ca(NO<sub>3</sub>)<sub>2</sub>, Na<sub>2</sub>SO<sub>4</sub>, CaCl<sub>2</sub>, and NH<sub>4</sub><sup>+</sup> cations containing electrolytes.<sup>[18]</sup> Next to the electrolyte, the synthesis suspension consists of a dispersed support material, corresponding mostly to Vulcan® carbon due to its high surface area, excellent electronic conductivity and/or sufficient chemical stability.<sup>[19,20]</sup> Several groups in the field of electrocatalysis elucidated electrochemical erosion to fabricate nanostructured catalysts based on different metals. Among others, those include Rh, Bi, Sn, Pb, Au, and Cu, synthesized by the groups of Li<sup>[21,22,23,24]</sup> and Koper.<sup>[18,25,26,27,28]</sup> Our group primarily focused on Pt alloys, like Pt<sub>x</sub>Pr<sup>[29]</sup> and pure Pt.<sup>[30]</sup> These Pt NPs exhibit better ORR activity than commercial catalysts.<sup>[31]</sup>

The electrochemical erosion approach allows to produce Pt-containing NPs with a single-digit nanometric diameter. At such particle dimensions, size and shape modifications can essentially dictate their adsorption properties, influencing the activity toward specific reactions. Driven by elucidating this size and shape effect of Pt NPs, Garlyyev et al. explored shape and size

variations via electrochemical erosion.<sup>[30]</sup> Nevertheless, in the past, Pd seemed inapplicable for these types of techniques. Yanson et al.<sup>[25]</sup> attributed this failure to the formation of a hydride layer at the Pd surface during electrochemical erosion. Later, Feng et al.<sup>[18]</sup> reported the synthesis of Pd nanostructures in 0.3 M CaCl<sub>2</sub>, but only with the indispensable presence of the surfactant polyvinylpyrrolidone (PVP). However, organic additives are known to contaminate the surface of the catalyst, which leads to a decrease in the catalytic performance of the synthesized catalyst. Furthermore, it is known that synthesizing nanostructures by electrochemical erosion without using surfactants leads to large agglomerations and highly polydisperse particles.<sup>[18,25]</sup> Despite these challenges, we present in this work the first surfactant-free synthesis of Pd NPs by electrochemical erosion, which leads to the production of single-digit nanometer-sized Pd NPs, homogeneously distributed on Vulcan Carbon, that significantly outperform a commercial reference Pd/C catalyst towards the hydrogen evolution reaction (HER).

## 2. Results and Discussion

### 2.1 Synthesis of Pd nanoparticles

To fabricate Pd NPs with a diameter below ten nanometers, we developed a surfactant-free synthesis procedure. Next to electrochemical erosion, the method involves two crucial steps, as depicted in **Figure 1a** and **1b**, which showcase the optimized two-step pretreatment approach of Pd wires employed in this study. The first step, displayed in Figure 1a, alters the structural properties of Pd due to the formation of palladium hydride (PdH<sub>x</sub>), e.g., during HER in acidic media. H atoms diffuse into the crystal structure of Pd and occupy octahedral voids,<sup>[32]</sup> which stresses the crystal structure and subsequently deform and embrittle the Pd wire.<sup>[33,34,35,36]</sup> The embrittlement is not restricted to the wire surface since it is well-known that hydrogen diffuses into sub-surface and bulk regions.<sup>[37]</sup> The second step, illustrated in Figure 1b, modifies the structural properties even further via an annealing and cooling treatment in an Ar atmosphere at ~ (950-1050)°C. Firstly, the annealing secures the absorbed hydrogen leaving the Pd bulk. Secondly, heat treatment with succeeding cooling of Pd forms terrace arrangements and deep grooves or cracks at grain boundaries located on the surface of the Pd wires.<sup>[38]</sup> Similarly, Yule et al.<sup>[39]</sup> performed flame-annealing with subsequent quenching in deionized water. They identified the resulting distortions in the grain boundaries of the Pd structure as hot spots for

hydrogen absorption through scanning electrochemical cell microscopy techniques (SECCM). Due to those hot spots, Pd wires absorb hydrogen more dominantly during HER, resulting in a bigger embrittlement effect originating from PdH<sub>x</sub> formation. Accordingly, to guarantee a maximal state of embrittlement, we individually repeated the HER and annealing pretreatment up to three times. Scanning electron microscopy (SEM) experiments clarified the effect of the two-step pretreatments by comparing the morphology of the Pd wire before and after the process, as well as after the erosion procedure, as illustrated in **Figure S1**. After performing the two-step pretreatment, we electrochemically eroded the rough Pd wires by immersing them in a suspension and applying an alternating potential signal. **Figure 1c** displays a scheme of the electrochemical erosion technique, which involves multiple parameters that are likely to affect the synthesized Pd NPs. These parameters include the type of wire pretreatment, NaNO<sub>3</sub> concentration in the electrolyte, and the applied erosion signals, such as frequency and amplitude. Initially, we conducted the two-step pretreatment once and varied the frequency of a  $\pm 25$  V applied sinusoidal voltage signal from 20 Hz to 200 Hz. A detailed summary of the obtained results can be found in the Supporting Information. Nevertheless, Pd NPs synthesized via a three-time repeated pretreatment with a  $\pm 25$  V, 200 Hz applied sinusoidal voltage signal in 1 M NaNO<sub>3</sub> electrolyte exhibited more promising results. The Transmission electron microscopy (TEM) image in **Figure 1d** depicts a rough overview of the synthesized Pd NPs and their homogeneous distribution on the Vulcan® carbon support. In the following part, we more profoundly elucidate their structural and compositional properties. The conducted characterizations include TEM, which more accurately describes NP dispersion on the support material. By using high-resolution transmission electron microscopy (HRTEM), scanning transmission electron microscopy (STEM) and STEM with energy dispersive X-ray spectroscopy (STEM-EDX), we investigated their size, shape and chemical composition, respectively.

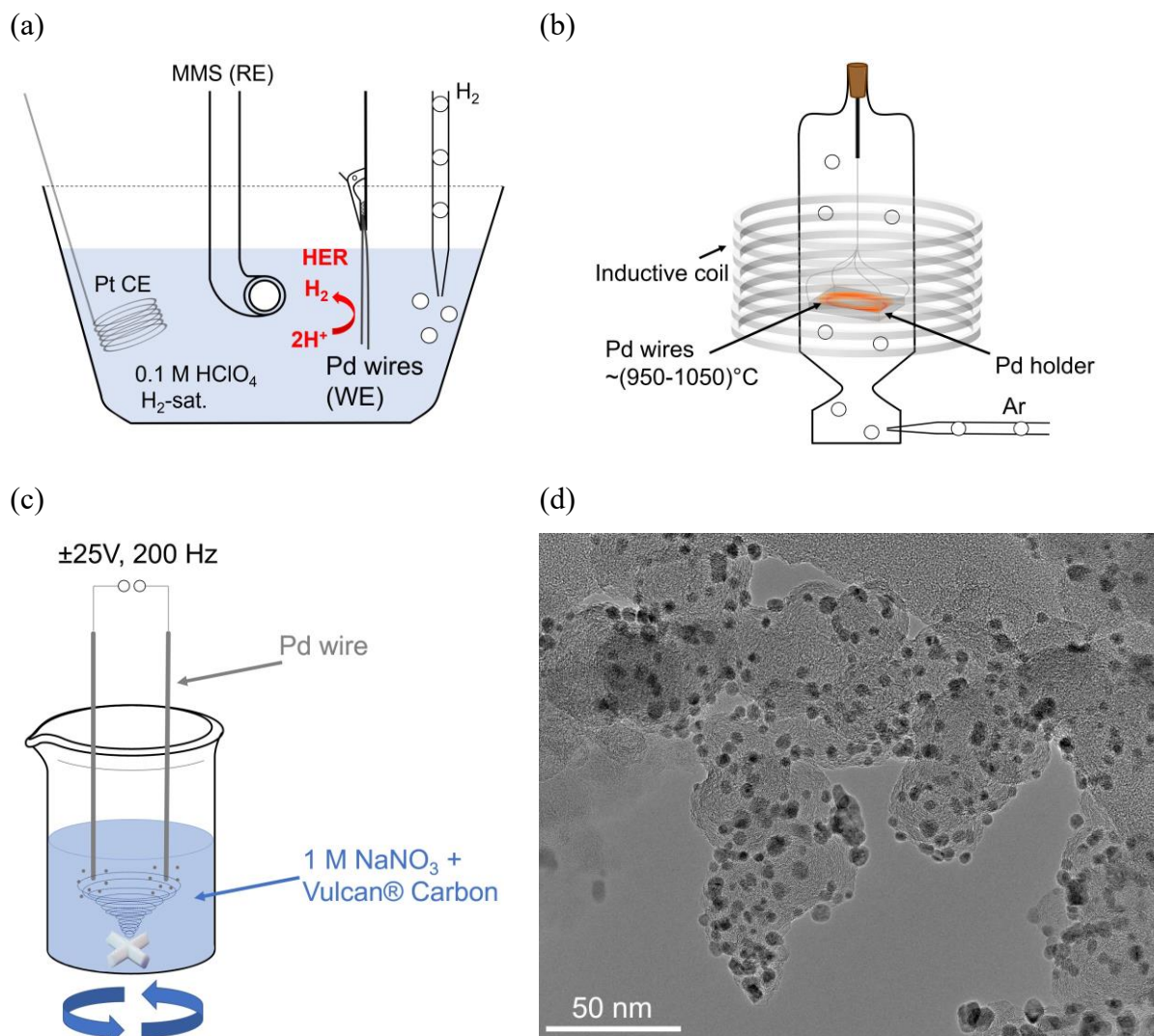


**Figure 1.** (a) Schematic of the HER pretreatment of Pd wires immersed in a three-electrode cell containing H<sub>2</sub>-saturated 0.1 M HClO<sub>4</sub> electrolyte. The Pd wires serve as a WE to produce molecular H<sub>2</sub> during cyclic voltammetry. (b) Schematic of the subsequent annealing pretreatment, displaying the annealed Pd at ~(950-1050) °C on a Pd holder in an inductive heater under an Ar atmosphere. (c) Schematic of the top-down electrochemical erosion approach. NPs formed due to the application of a ±25V, 200 Hz sinusoidal potential signal in a suspension containing 1 M NaNO<sub>3</sub> and dispersed Vulcan® carbon. (d) A TEM image of the Pd/C catalyst after synthesis.

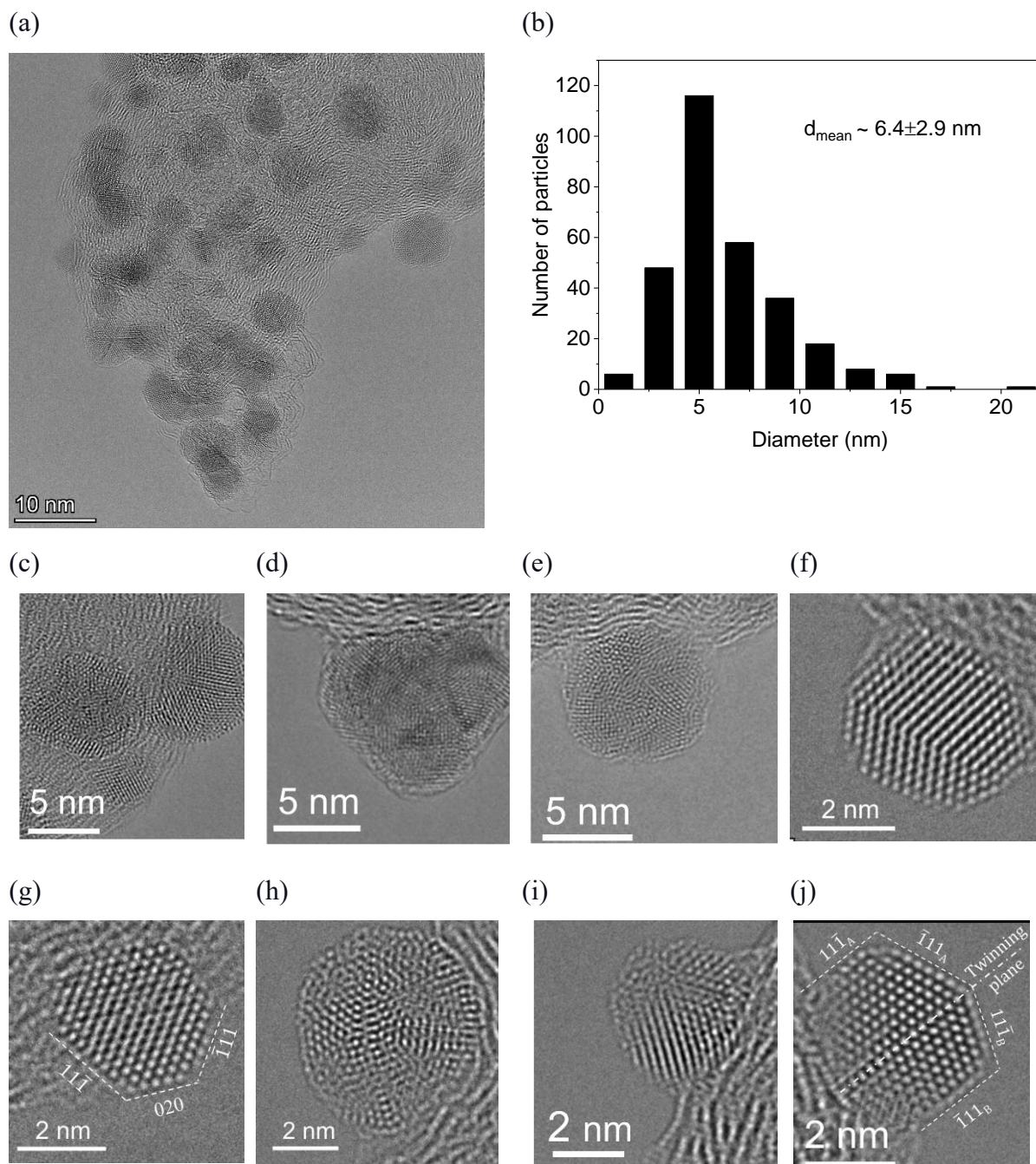


**Figure 2.** TEM investigation of the Pd/C catalyst synthesized in 1 M NaNO<sub>3</sub> with different resolutions. (a) A TEM overview image. (b) Histogram of the diameter distribution and mean diameter of the synthesized Pd NPs on C catalyst. (c-j) HR-TEM images of single Pd particles with atomic resolution. For (g and j) the Miller indexes of the respective lattice planes were added since, the NPs are well oriented to the (011) zonal axis.

## 2.2 Catalyst characterization by TEM, STEM, HRTEM, STEM-EDX and XPS

**Figure 2a** provides a magnified, atomically resolved view of the overview in Figure 1d. The high resolution validates the homogeneous distribution of the Pd NPs, even though certain areas exhibit a slightly higher density of NPs. **Figure 2b** presents a Pd NP size distribution and a mean average diameter of  $6.4 \pm 2.9$  nm, as measured from TEM and STEM images. In addition, **Figure 2c–2j** display HRTEM images of single Pd NPs. The particles reveal crystalline structure, and their sharp edges suggest a non-spherical but rather polyhedral shape. We emphasize that it is difficult to make conclusive results of the observed NPs polyhedron types from the images, however, they appear to form cubical up to complex polyhedron shapes (in the case of larger particles), as indicates the different number of facets revealed in the recorded images. Next to the TEM and HRTEM imaging of the structure, we used energy-dispersive X-ray spectroscopy (EDX) in STEM to create elemental maps of the Pd/C catalyst. The investigated elements include carbon, oxygen and palladium, as shown in **Figure 3a–3c**. **Figure 3b** reveals a homogeneous distribution of oxygen in the EDX map, which may arise either from the H<sub>2</sub>O<sub>2</sub> pretreatment of the Vulcan® XC72R or from atmospheric oxygen, which oxidized its surface and formed oxygen-containing functional groups at the surface.<sup>[40]</sup> The oxygen signals do not correlate with the positions of the Pd NPs, depicted in **Figure 3c**; only at the carbon edges some of the positions coincide. We highlight that detecting oxygen by EDX proves problematic if the oxygen is present in small concentrations, such as a thin oxidized shell around NPs. Therefore, X-ray photoelectron spectroscopy (XPS) measurements were conducted to identify the oxide contribution of the Pd/C catalyst more accurately. **Figure 3d** illustrates the analysis of 3d<sub>3/2</sub> and 3d<sub>5/2</sub> doublet of Pd<sup>0</sup> and Pd<sup>2+</sup> spectra, which refers to metallic and oxidized Pd, respectively. Calculating the peak areas, we estimated the atomic content of metallic Pd<sup>0</sup> at 70 % and Pd<sup>2+</sup> at 30 %. It is highly probable that a significant amount of the Pd<sup>2+</sup> forms during the erosion process due to strong anodic polarization, which significantly promotes oxygen evolution.

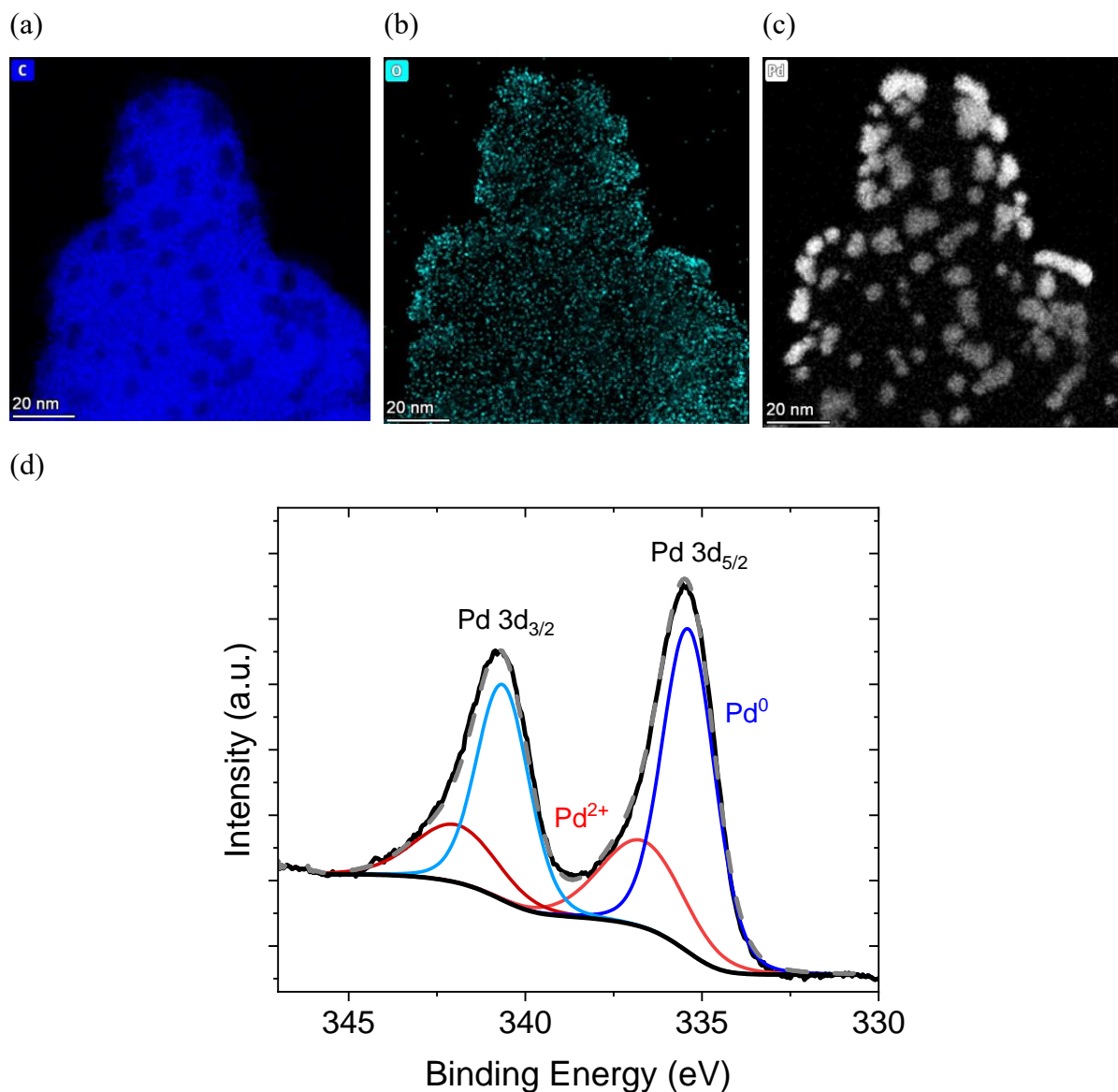


**Figure 3.** STEM-EDX of the Pd/C catalyst synthesized in 1 M NaNO<sub>3</sub> with elemental mapping of (a) C-K, (b) O-K, and (c) Pd-L. (d) XPS spectrum of the Pd/C catalyst. The Pd 3d peaks indicate the presence of Pd<sup>0</sup> and Pd<sup>2+</sup>, corresponding to metallic and oxidized Pd states, respectively.

### 2.3 Study of the electrolyte concentration on the Pd NPs synthesis using XRD

In the following section, we examine the effect of NaNO<sub>3</sub> concentration on the synthesized Pd NPs using X-ray diffraction (XRD) and electrochemical characterization. We produced three batches of Pd/C catalyst in 1 M, 2 M, and 4 M NaNO<sub>3</sub> by applying a  $\pm 25$  V, 200 Hz sinusoidal potential signal. **Figure 4a-4c** display the recorded diffraction patterns of the Pd/C catalysts fabricated in 1 M, 2 M, and 4 M NaNO<sub>3</sub>, including the corresponding Bragg peak positions.

Experimental diffraction profiles attributed to the Pd signal possess a non-trivial shape, which can hardly be described by a simple pseudo-Voigt profile. A closer look at the peak shape and its systematic broadening yields the model, which is based on two different Pd phases characterized by different weight fractions, crystallite size, and lattice parameters (colored in red and green) on top of the broad contribution from the H<sub>2</sub>O<sub>2</sub>-pretreated Vulcan® carbon XC72R in blue. It is hypothesized that two phases correspond to unstrained and strained Pd, where the strain could potentially originate from the harsh synthesis conditions of the Pd NPs. It must also be mentioned that the secondary (strained) Pd phase is present in non-negligible amounts and needs to be properly accounted. Applying a  $\pm 25$  V potential amplitude generates gaseous oxygen and hydrogen excessively, consequently causing irreversible deformation and stress within the Pd crystal structure. Alternatively, the strain could arise during the cathodic polarization of the wires if extensive quantities of atomic hydrogen irreversibly absorb into the Pd crystal lattice. This assumption agrees with the work of Zhao et al. and Benck et al., who observed similar signal patterns, including sub-peaks originating from hydride formation in the case of Pd-based materials.<sup>[41,42]</sup> The signal from non-strained (green) and strained (red) Pd NPs was modeled using the full-profile Rietveld method. Additionally, extra peaks emerged in the diffraction patterns for the Pd NPs synthesized in 4 M NaNO<sub>3</sub>, which we attributed to NaNO<sub>3</sub> residues in the corresponding batch. Following lattice parameters (0.39008 $\pm$ 0.00002 nm, 0.39044 $\pm$ 0.00002 nm, and 0.39082 $\pm$ 0.00003 nm) were detected for non-strained Pd components produced in 1 M, 2 M, and 4 M NaNO<sub>3</sub>, respectively. Contributions from strained Pd were characterized by slightly higher lattice parameters (0.39285 $\pm$ 0.00008 nm, 0.39224 $\pm$ 0.00010 nm, and 0.39309 $\pm$ 0.00012 nm for the corresponding PdH<sub>x</sub> NPs). Following the relation between the lattice parameter and H: Pd ratio in the PdH<sub>x</sub> beta phase from Zhao et al.,<sup>[43]</sup> the obtained H: Pd ratios correspond to  $\sim 0.17$ ,  $\sim 0.14$ , and  $\sim 0.18$  for the Pd catalysts synthesized in 1 M, 2 M, and 4 M NaNO<sub>3</sub>, respectively. Besides this, the weight ratio disparities between the two Pd phases was explored as well. In the case of the Pd/C synthesized in 2 M, and 4 M NaNO<sub>3</sub>, the difference between strained and non-strained Pd is relatively negligible. The strained Pd phase constitutes 48 wt% and 53 wt% of the total Pd content in the Pd/C catalyst fabricated in 2 M and 4 M NaNO<sub>3</sub>. In contrast to those batches, the Pd/C catalyst synthesized in 1 M NaNO<sub>3</sub> contains a larger proportion of strained Pd, correlating to roughly 63 wt%. Next to the weight ratio comparison of strained and non-strained Pd, we assessed their average crystallite size for the respective catalyst batches.<sup>[44]</sup> The crystallite sizes for strained and non-strained Pd differ significantly in each batch but remain comparable across the different Pd/C batches. For the NPs synthesized in 1 M NaNO<sub>3</sub>, the average crystallite sizes for strained and

non-strained Pd correspond to ~1.9 nm and ~6.1 nm. The average crystallite sizes for the Pd/C batches synthesized in 2 M and 4 M NaNO<sub>3</sub>, and a summary of all parameters extracted from XRD analysis can be found in **Table S1** and **S2**, in the Supporting Information.

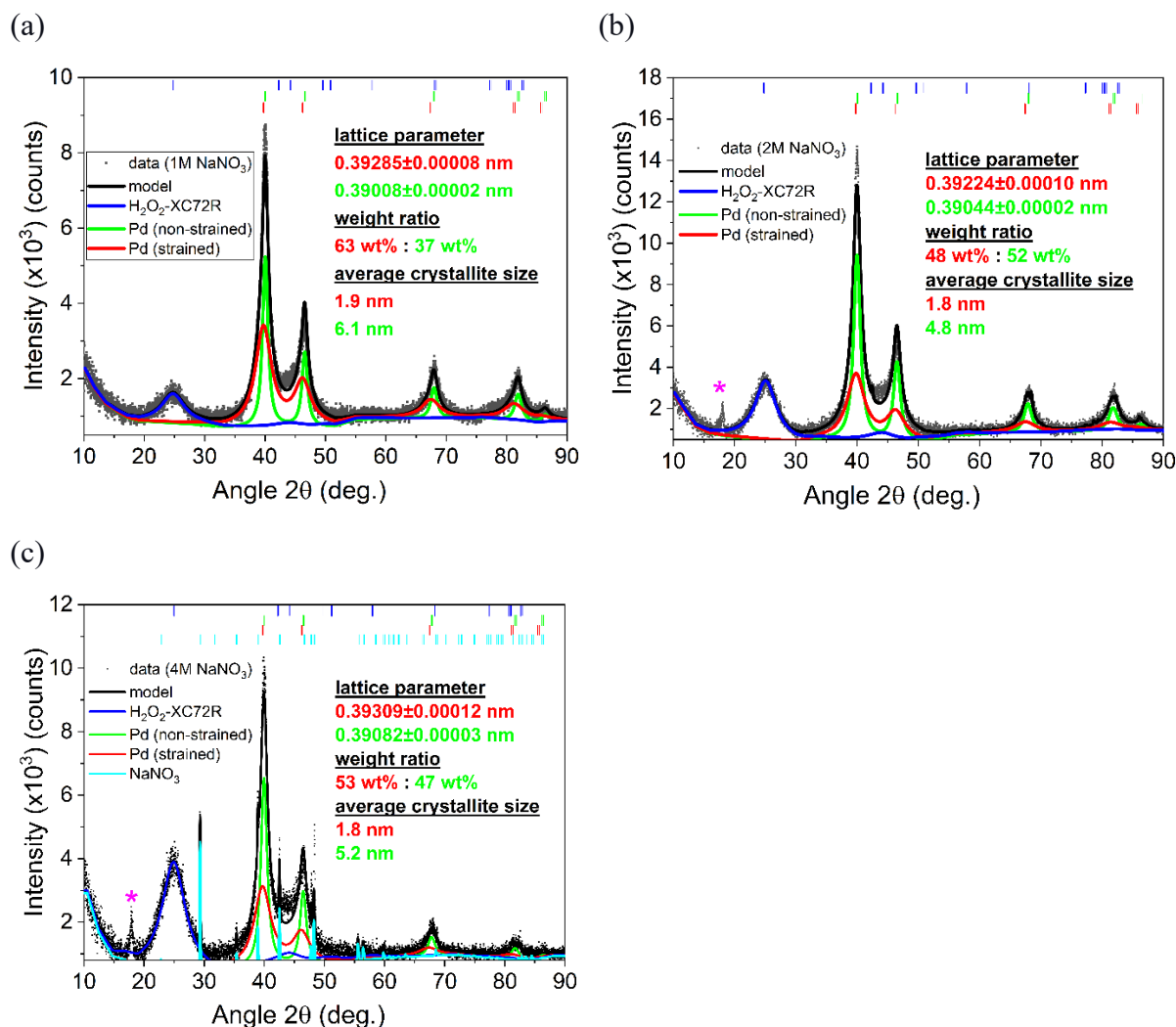


**Figure 4.** XRD patterns and Rietveld models of the Pd/C catalysts synthesized with  $\pm 25$ V amplitude, 200 Hz sinusoidal potential signal in (a) 1 M, (b) 2 M, and (c) 4 M NaNO<sub>3</sub> (black curve). The blue shaded area represents the fit of the H<sub>2</sub>O<sub>2</sub>-pretreated Vulcan® carbon in the pattern. The red and green sub-peaks correspond to the fit of the strained and non-strained Pd, respectively. The cyan sub-peaks can be attributed to the fit of NaNO<sub>3</sub> residues in the Pd/C catalyst. Purple \* correspond to an unidentified reflection.

## 2.4 Electrochemical Measurements.

**Figure 5a** displays the cyclic voltammograms (CVs) recorded in Ar-saturated 0.1 M HClO<sub>4</sub> for the synthesized samples in 1 M, 2 M, and 4 M NaNO<sub>3</sub>. Despite slight variations in mass loading, which are smaller than 3 %, the intensity of the H absorption/adsorption and H desorption peaks in the CVs increase with decreasing NaNO<sub>3</sub> concentration during synthesis. A similar tendency appears for the specific surface area (SSA), which increases almost linearly with a decrease in the electrolyte concentration. The lowest SSA of  $27.1 \pm 5.0 \text{ m}^2 \text{ g}_{\text{Pd}}^{-1}$  corresponds to the Pd/C

catalyst fabricated in 4 M NaNO<sub>3</sub>. Accordingly, the SSA increases to 58.9±3.5 m<sup>2</sup> g<sub>Pd</sub><sup>-1</sup> and 67.3±0.2 m<sup>2</sup> g<sub>Pd</sub><sup>-1</sup> for the catalysts manufactured in 2 M and 1 M NaNO<sub>3</sub>, respectively.

In our catalytic system, the SSA primarily varies with the size and shape of Pd NPs and their state of aggregation and distribution. Nevertheless, a larger SSA could modify the activity of the Pd/C catalyst for surface-sensitive reactions like the HER. This theoretical hypothesis coincides with our observations from the polarization curves conducted in H<sub>2</sub>-saturated 0.1 M HClO<sub>4</sub>, as displayed in **Figure 5b**. In the cathodic scan of the polarization curve, a characteristic peak occurs at slightly positive potentials, which is typical for Pd and relies on the formation of PdH<sub>x</sub>.<sup>[45]</sup> The geometric activity (GA) evaluated at -5 mV vs. RHE increases for the NPs prepared with decreasing NaNO<sub>3</sub> concentrations, starting with 0.44±0.18 mA cm<sub>geo</sub><sup>-2</sup>, 0.75±0.03 mA cm<sub>geo</sub><sup>-2</sup> and ultimately reaching 1.23±0.37 mA cm<sub>geo</sub><sup>-2</sup> for the Pd/C catalysts synthesized in 4 M, 2 M, and 1 M NaNO<sub>3</sub>, respectively.

Besides the GA evaluation, we investigate trends of the mass activity (MA) and specific activity (SA) in correlation with the used NaNO<sub>3</sub> synthesis electrolyte concentration of the Pd/C catalysts. **Figure 5c** relates the NaNO<sub>3</sub> synthesis concentration to the evaluated SA. For the Pd/C samples synthesized in 1 M, 2 M, and 4 M NaNO<sub>3</sub>, the SA evaluated at -5 mV vs. RHE corresponds to 0.11±0.03 mA cm<sub>Pd</sub><sup>-2</sup>, 0.09±0.01 mA cm<sub>Pd</sub><sup>-2</sup>, and 0.11±0.05 mA cm<sub>Pd</sub><sup>-2</sup>, respectively. Schmidt et al. correlated the strain in the crystal structure from subsurface hydride layers to the change in adsorption Gibbs free energy ( $\Delta G$ ) of the hydrogen intermediate for Pd.<sup>[37]</sup> As a result,  $\Delta G$  and, thus, the intrinsic HER activity depends on the number of subsurface hydride layers and the H:Pd ratio. Under consideration of the error bars of the SA reported in **Figure 5C**, its values match remarkably well for the catalysts synthesized in 1 M, 2 M, and 4 M NaNO<sub>3</sub>, which coincides with the comparable H:Pd ratio for the three catalysts mentioned above. **Figure 5D** depicts the dependence of the MA on the NaNO<sub>3</sub> synthesis electrolyte concentration. The MAs evaluated at -5 mV vs. RHE correspond to 71.4±21.5 mA mg<sub>Pd</sub><sup>-1</sup>, 52.0±1.9 mA mg<sub>Pd</sub><sup>-1</sup>, and 28.4±11.4 mA mg<sub>Pd</sub><sup>-1</sup> for the Pd/C catalysts synthesized in 1 M, 2 M, and 4 M NaNO<sub>3</sub>, respectively. The enhanced MA of the Pd/C catalyst synthesized in 1 M NaNO<sub>3</sub> can most likely be attributed to the larger SSA and the enhanced amount of strained Pd NPs of approximately 63 wt% compared to non-strained Pd NPs. This electrochemical characterization underlines the effect of the NaNO<sub>3</sub> synthesis concentration on the resulting SSA and HER activity.

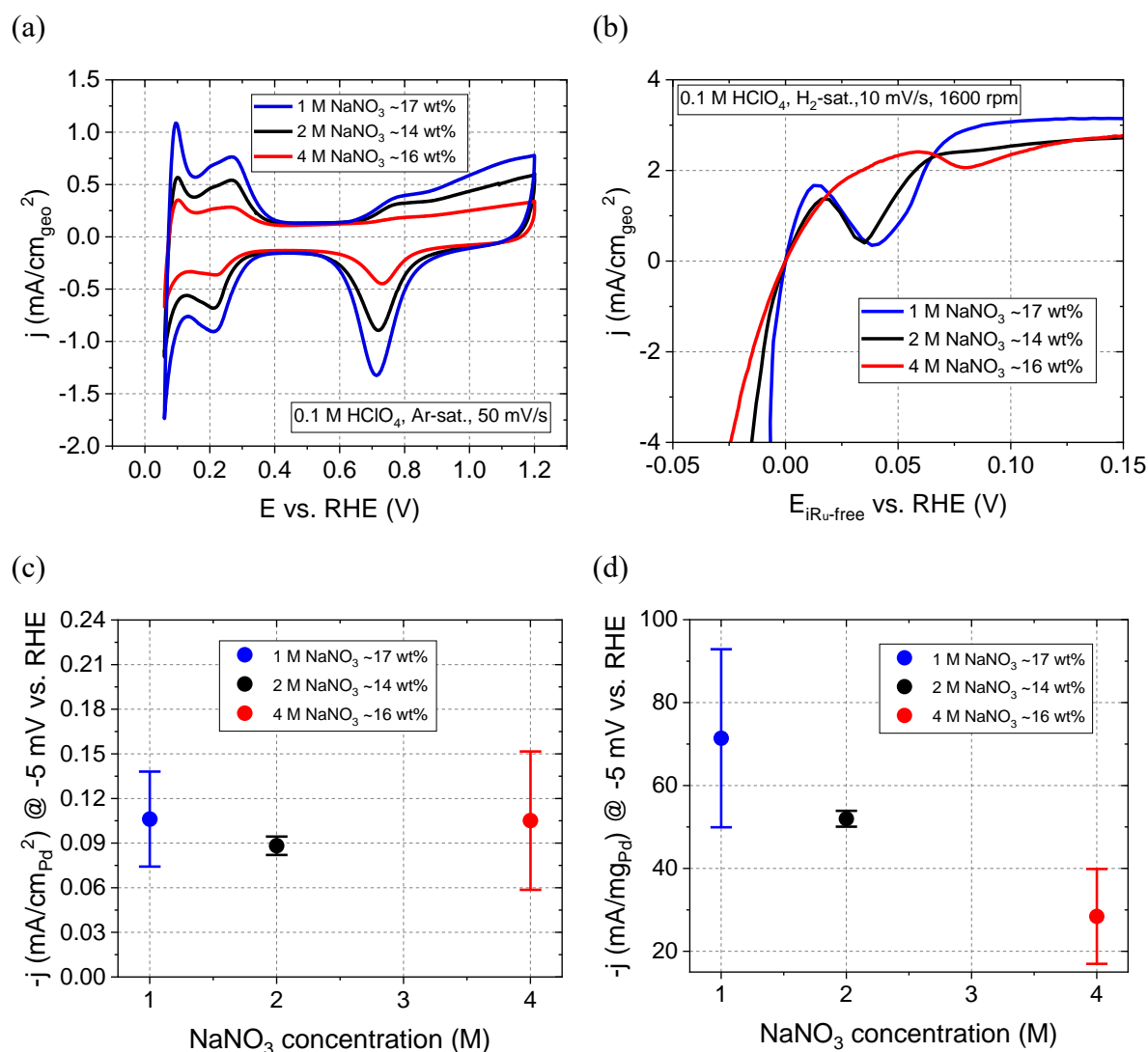


**Figure 5.** (a) CVs of Pd/C catalysts synthesized in NaNO<sub>3</sub> of various concentrations (1 M, 2 M, and 4 M). The curves were recorded in Ar-saturated 0.1 M HClO<sub>4</sub> at a scan rate of 50 mV s<sup>-1</sup> and rotation speed of 400 rpm. (b) Characteristic  $iR_u$ -corrected HER polarization curves (cathodic scan) of Pd/C catalysts, recorded in H<sub>2</sub>-saturated 0.1 M HClO<sub>4</sub> at a scan rate of 10 mV s<sup>-1</sup> and a rotation speed of 1600 rpm. Comparison of the (c) SA (d) MA evaluated at -5 mV vs. RHE with the NaNO<sub>3</sub> synthesis electrolyte concentration.

As a last step, we compared the electrochemical performance of our most active catalyst toward HER with a commercial 20 wt% Pd/C catalyst (brand: FC catalyst). For the FC catalyst, the Pd NPs are supported on Vulcan XC-72 and exhibit a crystallite size of 3-5 nm.<sup>[46]</sup> The crystallite size can be roughly treated as an approximation of the size of the nanoparticles which corresponds to our catalyst (**Table S2**), synthesized using the electrochemical erosion, top-down (TD) approach in 1 M NaNO<sub>3</sub>. For clarity, we will refer to our synthesized catalyst as Pd/C<sub>TD</sub> in the following section. As noted in the last paragraph, the SSA of the Pd/C<sub>TD</sub> catalyst corresponds to approximately 67.3±0.2 m<sup>2</sup> g<sub>Pd</sub><sup>-1</sup>, which is ~1.3 times greater than the SSA of the commercial FC catalyst, measured as 50.9±1.8 m<sup>2</sup> g<sub>Pd</sub><sup>-1</sup>. This difference in the SSA is apparent in the recorded CV profiles of both catalysts, displayed in **Figure 6a**. Across all peaks arising from faradaic processes, the peaks of the top-down synthesized Pd/C<sub>TD</sub> demonstrate higher currents. Regarding the HER activity, the Pd/C<sub>TD</sub> catalyst outperforms the commercial FC catalyst, as shown in the cathodic scans of the polarization curves (**Figure 6b**). The GA evaluated at -5 mV vs. RHE corresponds to 0.69±0.09 mA cm<sub>geo</sub><sup>-2</sup> and 1.23±0.37 mA cm<sub>geo</sub><sup>-2</sup> for the commercial Pd/C and Pd/C<sub>TD</sub> catalyst, respectively. As shown in **Figure 6c**, the MA of the Pd/C<sub>TD</sub> corresponds to 71.4±21.5 mA mg<sub>Pd</sub><sup>-1</sup> and is, therefore, ~2.2 times larger than the MA of 32.5±3.81 mA mg<sub>Pd</sub><sup>-1</sup> of the Pd/C FC catalyst. The SA follows a similar trend, with Pd/C<sub>TD</sub> revealing an activity of 0.11±0.03 mA cm<sub>Pd</sub><sup>-2</sup> and thus surpassing the SA of 0.06±0.02 mA cm<sub>Pd</sub><sup>-2</sup> of the commercial FC catalyst by 1.7 times. As discussed above, among other influences related to differences in size and shape of the Pd NPs, the intrinsic HER activity depends on the number of subsurface hydride layers and the H:Pd ratio of the Pd catalyst.<sup>[37]</sup> Due to the electrochemical erosion synthesis, strain emerges within the crystal structure of the Pd/C<sub>TD</sub>, which could significantly promote the formation of PdH<sub>x</sub> under reaction conditions, in contrast to the commercial Pd/C FC catalyst. This is evidenced by a distinct peak occurring at a slightly positive potential in the cathodic scan of the catalyst, indicating hydrogen absorption, which is undeniably more pronounced and broader for the Pd/C<sub>TD</sub> catalyst and could explain its higher activity due to PdH<sub>x</sub> formation.<sup>[37]</sup> In addition, durability tests of the two investigated catalysts were conducted by executing 1000 HER cycles for both catalysts, as displayed in **Figure 6d**. Over cycling, the commercial Pd/C catalyst demonstrated a progressive decline in current of the polarization curve, most likely due to the dissolution of Pd nanoparticles, a known phenomenon for Pd nanoparticles in

HClO<sub>4</sub> electrolyte.<sup>[47]</sup> In contrast, the Pd/C<sub>TD</sub> catalyst exhibited a current increase over the same number of cycles. To explain this difference between the two catalysts, we need to consider the peak occurring at slightly positive potentials in the cathodic scan once more, which is related to PdH<sub>x</sub> formation. For the commercial Pd/C FC catalyst, this absorption peak almost completely vanishes over the 1000 cycles, suggesting that hydrogen absorption by the crystal structure no longer occurs as the Pd NPs reach their maximal accessible H:Pd ratio. Conversely, for the Pd/C<sub>TD</sub> nanoparticles, the peak broadens over 1000 cycles, indicating that even more hydrogen is absorbed compared to the first cycle. This continual absorption of hydrogen is crucial to understanding the increase in HER activity since an increased H:Pd ratio and an expanded amount of Pd subsurface layers containing hydrogen enhance the HER activity, as mentioned above.<sup>[37]</sup> Furthermore, we mention that a part of the improvement could also be attributed to the continual reduction of PdO (30% in Pd/C<sub>TD</sub> as determined via the XPS analysis in Figure 3) under reducing potentials during cycling.

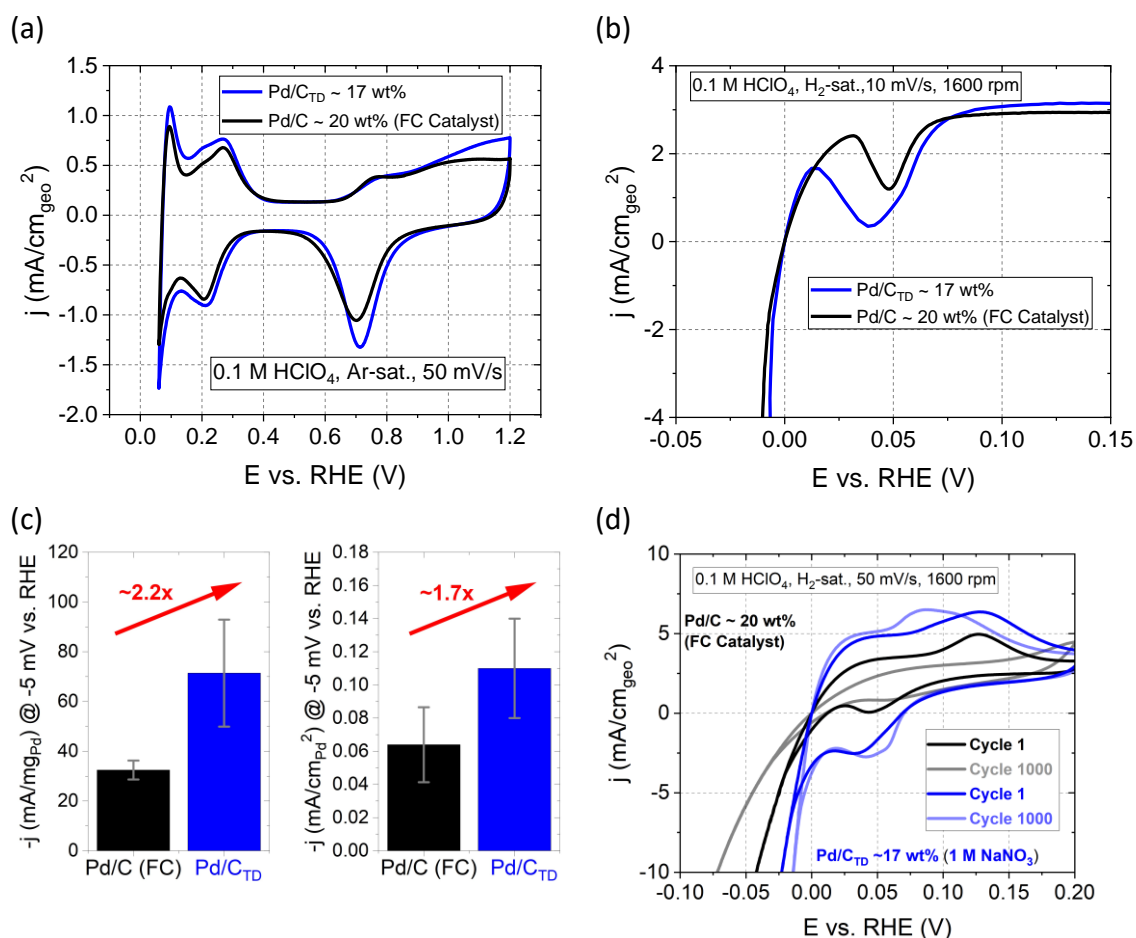


**Figure 6.** (a) CVs of the commercial Pd/C FC catalyst and the Pd/C<sub>TD</sub> catalyst synthesized in 1 M NaNO<sub>3</sub> by electrochemical erosion. The curves were recorded in Ar-saturated 0.1 M HClO<sub>4</sub> at a scan rate of 50 mV s<sup>-1</sup> and rotation speed of 400 rpm. (b) Characteristic *i*R<sub>u</sub>-corrected HER polarization curves (cathodic scan) of both catalysts, recorded in H<sub>2</sub>-saturated 0.1 M HClO<sub>4</sub> at a scan rate of 10 mV s<sup>-1</sup> and a rotation speed of 1600 rpm. (c) Comparison of the MA and SA evaluated at -5 mV vs. RHE of both catalysts. (d) Durability test by conducting 1000 HER cycles for both catalysts. The characteristic *i*R<sub>u</sub>-corrected HER polarization curves (cathodic and anodic scan) were recorded in H<sub>2</sub>-saturated 0.1 M HClO<sub>4</sub> at a scan rate of 50 mV s<sup>-1</sup> and rotation speed of 1600 rpm.

### 3. Conclusion

The synthesis of Pd nanostructures using electrochemical erosion without surfactants was not reported in the literature so far since the organic additives hinder the significant agglomeration processes for Pd. In our work, we developed a procedure based on the pretreatment method of Pd wires before electrochemical erosion and the choice of a suitable non-toxic electrolyte ( $\text{NaNO}_3$ ) that allowed us to synthesize homogeneously distributed, non-agglomerated nanoparticles supported on Vulcan® carbon. Furthermore, we discovered that the concentration of  $\text{NaNO}_3$  in the synthesis suspension significantly affects the properties of the formed NPs. Using 1 M  $\text{NaNO}_3$  leads to the formation of the most efficient NPs with a mean diameter of  $6.4 \pm 2.9$  nm and a SSA of  $67.3 \pm 0.2$  m<sup>2</sup> g<sub>Pd</sub><sup>-1</sup>. Electrochemical characterization toward the HER revealed a significant MA of  $71.4 \pm 21.5$  mA mg<sub>Pd</sub><sup>-1</sup> evaluated at -5 mV vs. RHE, which we attributed to an enhanced amount of strained Pd NPs of approximately 63 wt% compared to non-strained ones. In addition, we compared the activity and stability between the Pd/C catalyst synthesized in 1 M  $\text{NaNO}_3$  and a commercially available Pd/C catalyst. The results demonstrate that the Pd/C catalyst produced through electrochemical erosion outperforms the commercial catalyst in terms of MA and SA for the HER, exhibiting a ~2.2- and ~1.7-fold enhancement, respectively. During the stability tests, the activity of the commercial catalyst gradually declined, while the Pd/C catalyst synthesized via electrochemical erosion exhibited an increase in activity. This enhancement can be attributed to a continuous hydride formation process, effectively increasing the HER activity.

### 4. Experimental Section/Methods

*Vulcan® carbon XC72R pretreatment:* Despite working with aqueous electrolytes, we selected Vulcan® carbon XC72R as a support material. The oxidation of the Vulcan® carbon surface in an  $\text{H}_2\text{O}_2$  pretreatment step improves hydrophilicity and wettability.<sup>[40]</sup> For the pretreatment, Vulcan® XC72R (1 g) was dispersed in 30%  $\text{H}_2\text{O}_2$  (100 ml, 30%  $\text{H}_2\text{O}_2$ , p.a., ISO, Carl Roth, Germany) and continuously stirred for ~12h at ~70°C. Afterward, the stirred suspension was diluted with ultrapure  $\text{H}_2\text{O}$  (18.2 MΩcm, Merck Millipore, USA), followed by a filtering and

an H<sub>2</sub>O-washing step. The removal of water residues in the powder was accomplished by drying it at 60°C for ~16h.

*Electrochemical erosion:* Electrochemical erosion of bulk Pd wires ( $\varnothing = 0.25$  mm, 99.95%, MaTecK GmbH, Germany) generates active NPs, if the bulk wires undergo a pretreatment step to modify their properties beforehand. In our work, these modifications consist of an HER pretreatment, followed by an annealing pretreatment of the Pd wires. The HER step involves cyclic voltammetry conducted with Pd wires in a three-electrode cell filled with 0.1 M HClO<sub>4</sub> (70% HClO<sub>4</sub>, extra pure, Acros, Germany). The electrolyte was purged for 30 min with H<sub>2</sub> gas (5.0, Westfalen, Germany) to avoid undesired gaseous compounds and ensure stable equilibrium potential conditions. Further, 100 potential cycles with a scan rate of 50 mV s<sup>-1</sup> were executed with vertex potentials of 0.82 V and -0.38 V vs. RHE. Potentials lower than 0 V vs. RHE evolve molecular hydrogen, which partially absorbs and therefore induces stress in the Pd crystal structure. Subsequently, these hydrogen-containing Pd wires were annealed in an inductive heater (20-80 kHz, 15 kW, SP-15A, MTI, USA). Inside the heater, an Ar (5.0, Westfalen, Germany) atmosphere hinders Pd-oxide formation during annealing up to 900-1050°C for five cycles of 90 seconds. Between instances, 5-minute breaks with persistent Ar flow guarantee rapid cooling of the wires. During annealing, the absorbed hydrogen escapes from the Pd wires, leading to defects in the Pd bulk and surface. In addition, structural changes arise during the rapid cooling afterward, which is discussed in the results section. To increase the density of structural defects, we repeated the HER and annealing pretreatment either once or thrice for each wire. During electrochemical erosion, a potential was applied to Pd wires immersed in a suspension to produce NPs at their surface. The suspensions consisted H<sub>2</sub>O<sub>2</sub>-pretreated Vulcan® XC72R (~20 mg) dispersed in a NaNO<sub>3</sub> (ACS, ISO, Reag. Ph Eur, Merck, Germany) electrolyte solution. Further, ethanol (5 ml, EMSURE® ACS, ISO, Reag. Ph Eur, Sigma Aldrich®, USA) was added to enhance the Vulcan® carbon's hydrophilic character and ensure its excellent dispersion next to ultrasonication treatments. Parameters like the NaNO<sub>3</sub> concentration of the suspension affect the NP formation process. Accordingly, by applying a  $\pm 25$  V, 200 Hz sinusoidal AC voltage profile to Pd wires, NPs were synthesized in suspensions with NaNO<sub>3</sub> concentrations of 1 M, 2 M, and 4 M under continuous stirring of ~500 rpm. The effect of frequency variations was investigated in 1 M NaNO<sub>3</sub> suspensions applying a  $\pm 25$  V, sinusoidal AC voltage profile with 20 Hz, 100 Hz, or 200 Hz. Comparable mass loadings of the different samples arise by continuous erosion, until the mass of the initial Pd wires diminished by approximately 5 mg. This mass of synthesized Pd NPs results in a 20 wt% theoretical mass loading of the Pd/C catalyst since the synthesis suspensions consist of ~20 mg H<sub>2</sub>O<sub>2</sub>-pretreated

Vulcan® XC72R. After the synthesis, the mixture was stirred at 500 rpm for 16 h. Subsequently, the suspension was filtered in a Büchner funnel, washed with a mixture of ultrapure water and ethanol, and dried in a furnace at 60°C for 12 h.

*Catalyst Inks:* Several characterization methods rely on catalyst inks produced with the catalyst powder. These inks consist of Pd/C (10 mg), ultrapure H<sub>2</sub>O (3600 µl), isopropanol (1446 µl, puriss. p.a., ACS reagent, ≥ 99.8%, Sigma Aldrich®, USA), and Nafion® dispersion (30 µl, 5 wt% in lower aliphatic alcohols and water, Sigma Aldrich®, USA).

Consecutively, a 5 min ultrasonication treatment ensures a homogeneous distribution of the nanostructured catalyst.

*Thermogravimetric analysis:* For thermogravimetric analysis (TGA), a Mettler Toledo TGA instrument determines the Pd to-carbon support weight ratio of the Pd/C catalyst powder by recording the sample's mass versus time for a predefined temperature profile. The profile consists of three main steps: removal of residual water at 135 °C in Ar, carbon oxidation at 800°C in O<sub>2</sub> with simultaneous Pd oxide formation, and Pd oxide reduction at 800°C in Ar. For the steps at 800°C, the temperature was held constant for 30 min per step. The heating speed and gas airflow correspond to 50 K min<sup>-1</sup> and 50 mL min<sup>-1</sup>, respectively.

*Characterization:* Powder XRD provides the crystallographic and structural properties of the synthesized Pd/C nanostructured catalyst. For this purpose, the samples were illuminated with a Cu-Kα ( $\lambda = 1.5406 \text{ \AA}$ ) source with an integrated Ni-based filter by a Rigaku MiniFlex 600-C. The device records diffraction patterns in a slow-scanning mode with a (5° min<sup>-1</sup>) step velocity from 5° to 90°. Data analysis was performed applying full-profile Rietveld method as implemented in the program FullProf.<sup>[48]</sup> Contribution to diffraction patterns were modeled assuming isotropic size distribution, instrumental resolution was determined from Si reference measurements.

The TEM analysis was used for the Pd/C catalyst synthesized in 1 M NaNO<sub>3</sub> and ±25 V, 200 Hz sinusoidal AC voltage signal to visualize the morphology and chemical composition of the synthesized nanostructure in high resolution. The TEM was performed with an image spherical aberration corrected TITAN Themis 60-300 (Thermo Fischer Scientific, USA) microscope operated at 300 keV. The analysis was conducted via HRTEM imaging with spherical aberration corrected to ~0 µm, STEM imaging with a high-angle annular dark-field (HAADF) detector, and STEM-EDX elemental mapping with SUPER-X spectrometer. The STEM-EDX

maps of C-K, O-K and Pd-L were created by quantification of the collected shell signal of the elements with use Cliff-Lorimer k-factors<sup>[49]</sup> to weight %. All TEM data acquisition and processing was done with a software Velox v. 2.14. The size of the NPs was estimated using a software ImageJ.<sup>[50]</sup> In addition, the Pd NPs synthesized with 1 M NaNO<sub>3</sub> and  $\pm 25$  V AC voltage signal with 200 Hz, 100 Hz, and 20 Hz, were visualized by TEM. It was performed using a Jeol 2010 (CMTC-INPG) microscope with a LaB<sub>6</sub> filament and operating at 200 kV, with a 0.19 nm point to point resolution. The images were collected with a 2018  $\times$  2048 pixels CCD camera (Gatan Ultrascan 1000 XP).

XPS elucidates the catalysts' elemental composition and chemical state, including content estimations. The XPS device consists of a SPECS XR 50 (SPECS, Germany) X-ray source with a non-monochromatized Al K-alpha anode (1486.61 eV) and a PHOIBOS 150 hemispherical energy analyzer (SPECS, Germany) with a 150 mm mean radius. All spectra were acquired in an ultra-high vacuum chamber at an operating pressure below  $5 \times 10^{-9}$  mbar. The recorded XPS data was evaluated using the Casa XPS software (Version 2.3.25rev1.1J).

*Electrochemical measurements:* Pd/C catalysts are electrochemically characterized in a three-electrode setup consisting of the reference (RE), the counter (CE), and the working electrode (WE). Those electrodes were immersed in 0.1 M HClO<sub>4</sub> electrolyte within a glass cell previously cleaned with Caro's Acid / boiling water. This prevailing cleaning procedure consists of a 3:1 mixture of sulfuric acid (96% H<sub>2</sub>SO<sub>4</sub> Suprapur, Merck, Germany) and H<sub>2</sub>O<sub>2</sub>. The acidic mixture remains in the glass cells for approximately 12h. Following that, the glassware was washed several times with boiled ultrapure water.

A mercury/mercurous sulfate electrode (MMS) (Si Analytics, Germany) was used as a RE in our experiments. The CE consists of a multiple-circled Pt wire, predominantly owing to its high electrical conductivity, mechanical robustness, and excellent electrocatalytic activity.<sup>[51]</sup> The WE includes a rotating disc electrode (RDE) consisting of an OrigaTrod electrode rotator (OrigaLys ElectroChem SAS, France) and a suitable electrode tip. The tip comprised a 5 mm glassy carbon disk shielded by a PEEK (polyether ether ketone) coverage, hindering the exposure of glassy carbon edges or side surfaces. This configuration guarantees a well-defined geometric glassy carbon surface on which the aforementioned electrocatalyst inks (10  $\mu$ L) were drop-casted. Before ink deposition, the glassy carbon tips were polished with 1.0  $\mu$ m, 0.3  $\mu$ m, and 0.05  $\mu$ m grain-sized alumina paste (MicroPolish<sup>TM</sup>, Buehler, USA). After ink deposition, the hot air of a heat gun (D5950 Remington, Germany) dried the ink under persistent rotation.

The synthesized Pd/C catalysts were electrochemically characterized by applying different CV techniques. Those include voltammetry in Ar- and H<sub>2</sub>-saturated electrolytes. For this, we purged the 0.1 M HClO<sub>4</sub> electrolyte with Ar for 30 min to ensure the absence of O<sub>2</sub>. Subsequently, we executed the measurement at a scan rate of 50 mV s<sup>-1</sup> and a rotation speed of 400 rpm until reaching a steady state in the potential window between 0.06 and 1.2 V vs. RHE.

Further, to determine the *EC*SA, the CO-stripping method was used. For this method, purging 0.1 M HClO<sub>4</sub> with CO (1000 ppm CO in Ar, 4.7/5.0, Westfalen, Germany) for 15 min secures a CO-saturated electrolyte. Due to the lengthy purging procedure with CO, applying 0.1 V vs. RHE for 50 min under 400 rpm forms a CO monolayer with maximal coverage on the catalyst surface. Subsequently, the electrolyte was purged with Ar for 15 min before two CV cycles were executed with a scan speed of 10 mV s<sup>-1</sup> without rotation in the potential window between 0.06 and 1.2 V vs. RHE. The CO-stripping experiment defines the CO oxidation charge, which needs to be divided by the adsorbed CO surface coverage and the oxidation charge of a CO monolayer per unit area.<sup>[ 52 ]</sup> Both parameters significantly depend on the crystal orientation,<sup>[53,54]</sup> thus, making the situation difficult for polycrystalline nanoparticles. With the simplification in mind, we follow other reports and assume a CO surface coverage of 1 and a CO desorption per unit area of ~420 μC cm<sub>Pd</sub><sup>-1</sup>.<sup>[55]</sup> Furthermore, the *EC*SA was normalized by the determined Pd mass of the ink coatings deposited on the glassy carbon. This normalization results in the *SSA* and is essential for nanostructured electrocatalysts with different mass loadings.

For the HER/HOR polarization curve measurements, the 0.1 M HClO<sub>4</sub> electrolyte was continuously purged with H<sub>2</sub> for 30 min to saturate the electrolyte. The H<sub>2</sub>-saturation guarantees stable equilibrium potential during the cycling with a scan rate of 10 mV s<sup>-1</sup> and a rotation speed of 1600 rpm in the potential window of 0.82 V to -0.13 V vs. RHE. Since negative RHE potentials evolve hydrogen, we evaluated the HER activity at -5 mV vs. RHE from the cathodic polarization curve, which was additionally corrected for the scan rate. Furthermore, the measured potentials of the polarization curves were *iR<sub>u</sub>* corrected with the help of electrochemical impedance spectroscopy (EIS). The uncompensated resistance is determined by frequency perturbation of the applied potential in the 100 kHz to 10 Hz range with a 25 mV perturbation amplitude at different potentials. The EIS measurements were conducted in Ar-saturated 0.1 M HClO<sub>4</sub> under rotation of 1600 rpm.

Furthermore, the HER activities, evaluated at -5 mV vs. RHE, are presented as *SA* and *MA*. For the former, the measured current is normalized by the *EC*SA obtained from the CO-stripping

measurement. For the latter, the current is divided by the mass of the Pd NPs present in the ink coating on the glassy carbon.

For the durability test consisting of 1000 HER cycles, the 0.1 M HClO<sub>4</sub> electrolyte was continuously purged with H<sub>2</sub> for 30 min. The CVs were executed within a potential window of 0.22 V to -0.13 V vs. RHE with a scan rate of 50 mV s<sup>-1</sup> and rotation speed of 1600 rpm.

### **Supporting Information**

Supporting Information is available from the Wiley Online Library or from the author.

### **Acknowledgements**

We want to thank S. Schreier and X. Ma for their help with the conducted SEM and XRD experiments, respectively. This work has received funding from the European Union's Horizon 2020 research and innovation programme under grant agreement HERMES No 952184. Financial support from the German Research Foundation (DFG) under Grant No. 355784621, under Germany's Excellence Strategy-EXC 2089/1-390776260, under Germany's Excellence cluster "e-conversion" and DFG project BA 5795/6-1 is gratefully acknowledged. CzechNanoLab project LM2018110 funded by MEYS CR is gratefully acknowledged for the financial support of the TEM measurements at CEITEC Nano Research Infrastructure. P.M.S. and A.S.B are thankful for the funding via the Excellence Strategy of the Federal Government and the Länder in the context of the ARTEMIS Innovation Network.

Received: ((will be filled in by the editorial staff))

Revised: ((will be filled in by the editorial staff))

Published online: ((will be filled in by the editorial staff))

### Conflict of Interest

The authors declare no conflict of interest.

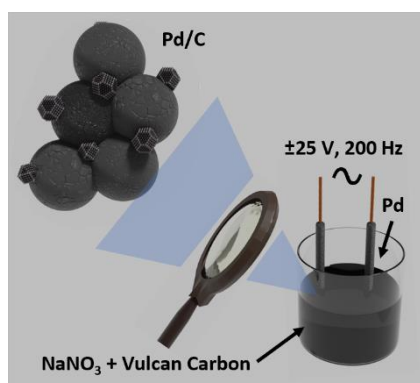
### Data Availability Statement

The data that support the findings of this study are available from the corresponding author upon reasonable request.

Christian M. Schott, Peter M. Schneider, Kais Sadraoui, Kun-Ting Song, Batyr Garlyyev, Sebastian A. Watzele, Jan Michalička, Jan M. Macak, Arnaud Viola, Frédéric Maillard, Anatoliy Senyshyn, Johannes A. Fischer, Aliaksandr S. Bandarenka\*, Elena L. Gubanova\*

### Top-Down Surfactant-Free Synthesis of Supported Palladium Nanostructured Catalysts

A surfactant-free top-down approach, called “electrochemical erosion”, allows the fabrication of palladium (Pd) nanoparticles (NPs) supported on Vulcan® Carbon. Crucially, a Pd wire pretreatment is identified as the essential step to synthesize NPs with sizes below 10 nm. The synthesized Pd/C catalysts are thoroughly analyzed for their structure, morphology, chemical composition, and electrochemical activity toward the hydrogen evolution reactions.



## Supporting Information

**Top-Down Surfactant-Free Synthesis of Supported Palladium Nanostructured Catalysts**

*Christian M. Schott, Peter M. Schneider, Kais Sadraoui, Kun-Ting Song, Batyr Garlyyev, Sebastian A. Watzele, Jan Michalička, Jan M. Macak, Arnaud Viola, Frédéric Maillard, Anatoliy Senyshyn, Johannes A. Fischer, Aliaksandr S. Bandarenka\*, Elena L. Gubanova\**

To synthesize Pd nanoparticles (NPs), we applied a  $\pm 25$  V sinusoidal AC potential signal to bulk Pd wires immersed in a suspension containing an electrolyte and the carbon support. The choice of an appropriate electrolyte is mandatory since the respective ions drastically affect the erosion of bulk wires. The technique demonstrates various methodological parameters, like electrolyte concentration and the frequency of the sinusoidal AC potential. Both parameters directly influence the properties of the synthesized Pd NPs.

The most elaborated NP formation theory attributes the critical role in this process to the cation of the electrolyte.<sup>[56]</sup> Nevertheless, in the case of Pd, we found that the anion significantly influences the electrochemical erosion process. Under application of a  $\pm 25$  V, 200 Hz sinusoidal potential signal, erosion failed in 1 M sodium carbonate ( $\text{Na}_2\text{CO}_3$ ), acetate ( $\text{C}_2\text{H}_3\text{NaO}_2$ ), perchlorate ( $\text{NaClO}_4$ ), and sulfate ( $\text{Na}_2\text{SO}_4$ ); but succeeded in sodium nitrite ( $\text{NaNO}_2$ ) and nitrate ( $\text{NaNO}_3$ ).

For  $\text{NaNO}_2$ , the formed NPs rapidly agglomerated after production, prohibiting any catalytic application. In the case of  $\text{NaNO}_3$ , we did not detect notable particle agglomeration after erosion. Nevertheless, we highlight that the wires in  $\text{NaNO}_3$  only erode if they already exhibit a rough surface containing numerous defects. The roughness of the wires can result from various pretreatment strategies. Hence, we invented a wire pretreatment process, which tremendously improved the erosional behavior of Pd wires for the reproducible synthesis of Pd NPs in a  $\text{NaNO}_3$  electrolyte. SEM experiments clarified the effect of the two-step pretreatment by comparing the morphology of the Pd wire before and after the process, as illustrated in **Figure S1a** and **S1b**, respectively. Initially, the pristine surface exposes multiple deep grooves and cracks next to flat areas with significant size. After pretreatment, the flat areas disappeared,

and simultaneously, the amount of visible deep grooves or cracks drastically increased. Additionally, slightly larger surface areas appear rough, presumably emerging from multiple nano-grooves or cracks that cannot be visualized due to the limited resolution of the SEM. Furthermore, **Figure S1c** magnifies the surface after the pretreatment and indicates that the grooves or cracks develop at grain boundaries. We assume that erosion occurs at those grooves at the grain boundary due to the large defect density in this distorted region. Additional SEM measurements after erosion validate this hypothesis since the grooves at grain boundaries significantly enlarge during the erosion, as depicted in **Figure S1d**. Due to the large grooves, plateaus are visible on the entire surface, as shown in the inset of Figure S1d, which correspond to the initial grains of the Pd wire.

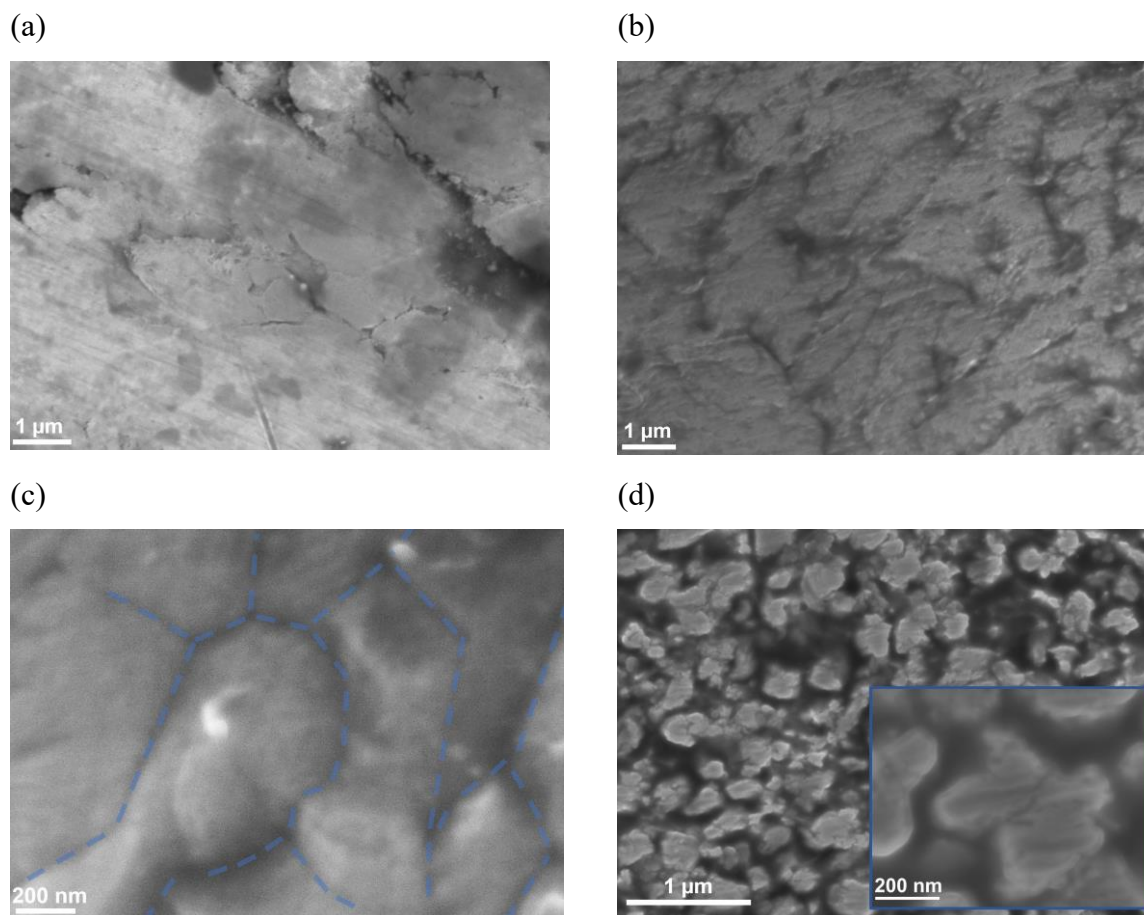


**Figure S1.** SEM images of (a) a pristine Pd wire and (b) the same wire after the pretreatment procedure. (c) Magnification of (b) to illustrate that the Pd wire cracks at the grain boundaries. (d) SEM image of the pretreated wire after the erosion with a  $\pm 25$  V, 200 Hz sinusoidal potential signal in 1 M  $\text{NaNO}_3$ . The inset magnifies the surface (d) after erosion.

Alternatively, to variation in the  $\text{NaNO}_3$  concentration, we investigated the effect of the frequency on Pd NP formation. Therefore, three batches in 1 M  $\text{NaNO}_3$  were fabricated by applying a  $\pm 25$  V sinusoidal potential signal with 200 Hz, 100 Hz, and 20 Hz frequency. As highlighted in the experimental part, the Pd wires for this synthesis were only treated once by the HER and annealing procedure. For morphological information, we executed TEM characterization of the Pd/C catalysts fabricated with 200 Hz, 100 Hz, and 20 Hz frequency, shown in **Figure S2a-S2d**. Two different types of particles coexist in all three elucidated samples. Firstly, small individual particles can be found, for which we estimate a diameter of  $\sim 7$ -8 nm. Secondly, large NPs with a diameter of roughly 30 nm are detected. For all samples, we created size distribution histograms distinguishing between the small and bigger NPs, as shown in **Figure S3a-S3c**. For the bigger Pd NPs synthesized with 200 Hz, 100 Hz, or 20 Hz frequency, the size corresponds to  $31 \pm 11$  nm,  $25 \pm 8$  nm, and  $33 \pm 11$  nm, respectively. For the

smaller Pd NPs, the size changes even less noticeably from  $7.0\pm 2.0$  nm to  $8.0\pm 2.0$  nm to  $8.0\pm 3.0$  nm, respectively. Besides the Pd NP size, the mass activity (*MA*) depends on the NP's shape and the defect density or roughness factor. Regarding the shape of the NPs, the recorded TEM images again reveal two different types of particles, which can explain the dissimilar *MA* reported above. For the Pd/C catalyst synthesized with 200 Hz frequency (Figure S2a), the Pd NPs display smooth surfaces without observable defect states. However, for the Pd/C catalyst produced with 100 Hz and 20 Hz frequencies (Figure S2b and S2c), the particles emerge in a "cloudy" formation without smooth surfaces of significant size. The surface appears scattered, indicating a large density of defect states.

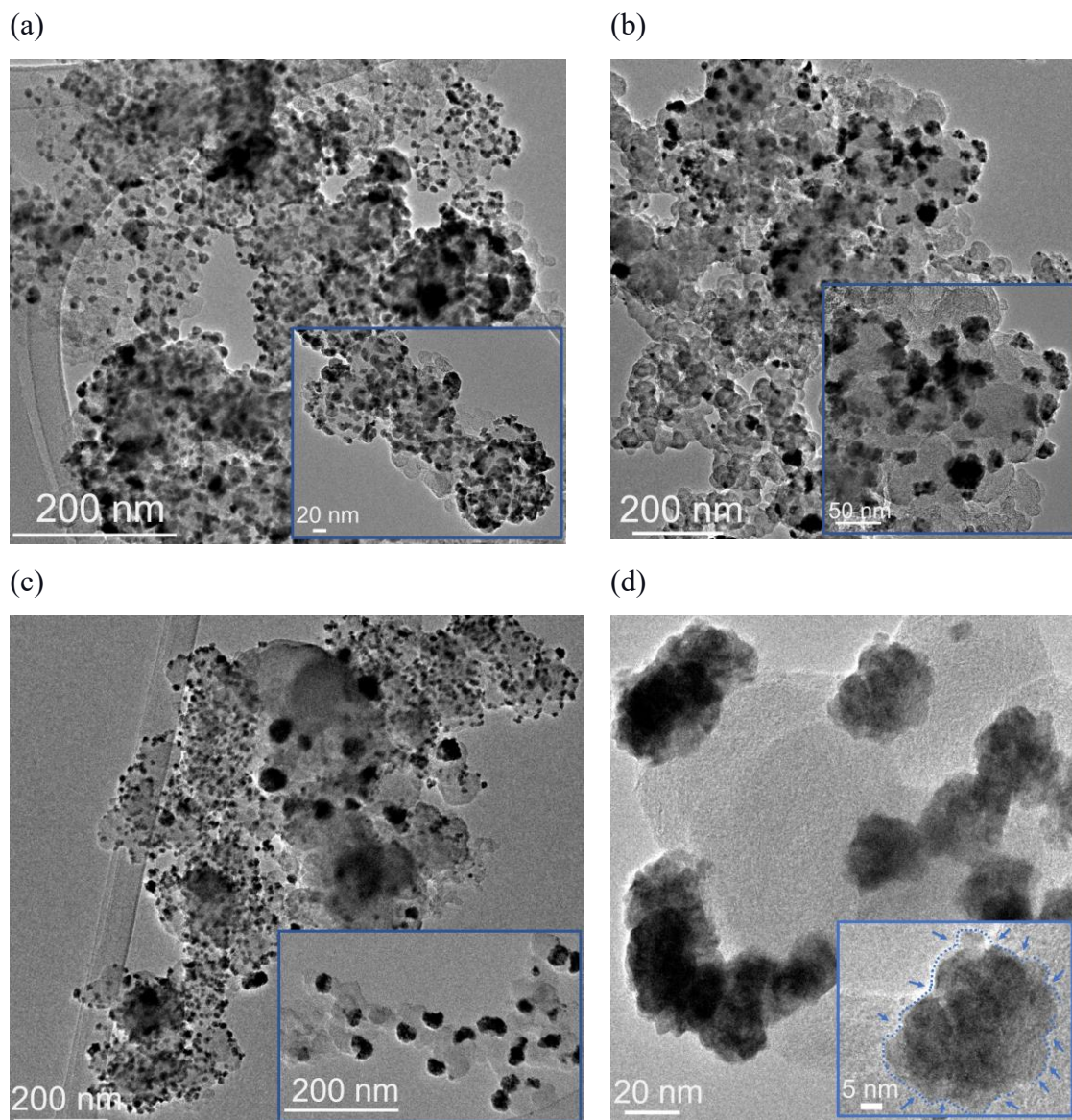


**Figure S2.** TEM images of the Pd/C catalysts synthesized with (a) 200 Hz, (b) 100 Hz, and (c)-(d) 20 Hz frequency with 200 nm and 20 nm resolution scale bars, respectively. The inset in (d) shows a single particle with a 5 nm resolution scale bar. The dashed line indicates the "cloudy" shape of the NP. The blue arrows point to concave-like defects.

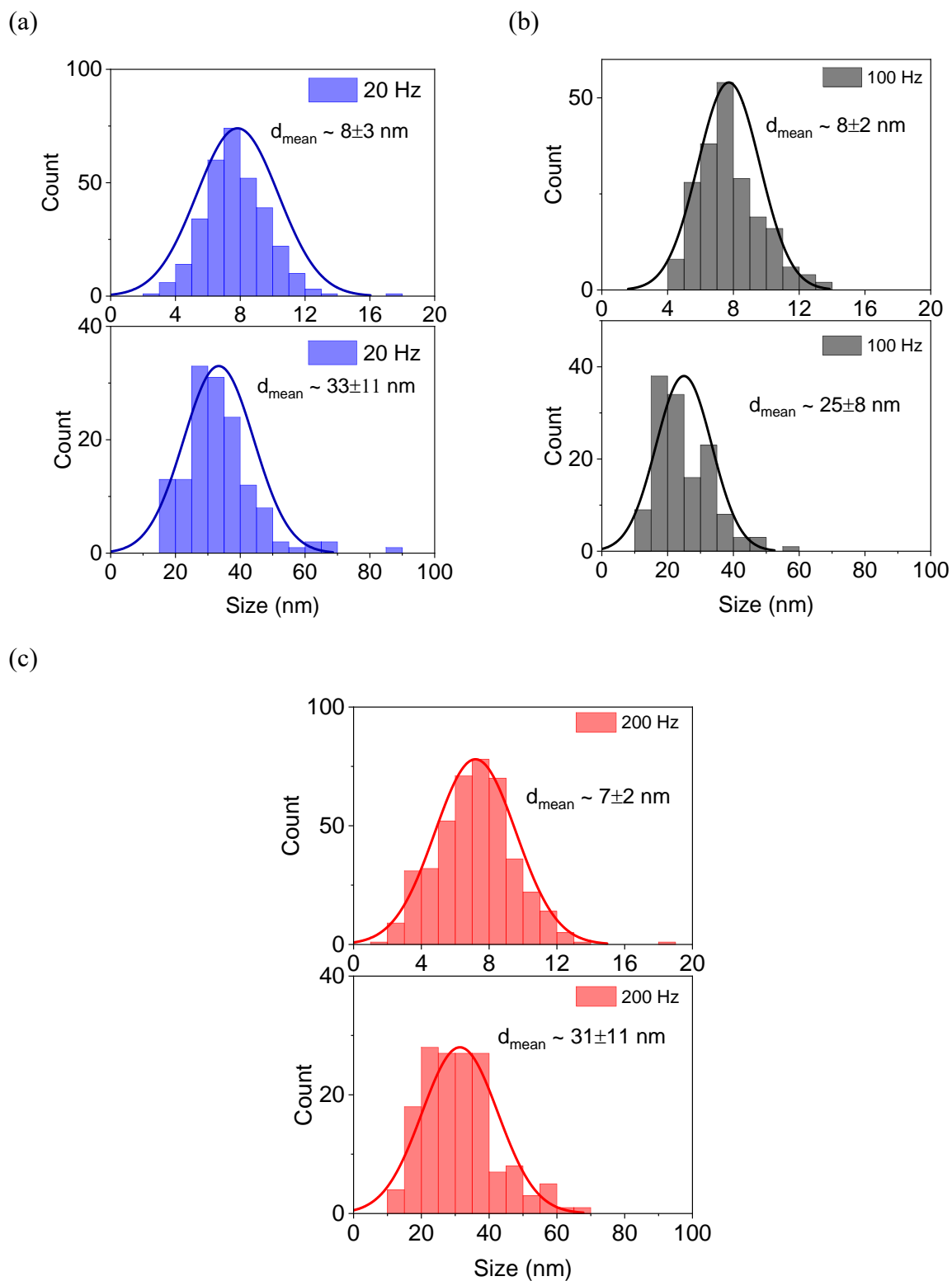


**Figure S3.** Distribution of the Pd NPs synthesized with (a) 20 Hz (b) 100 Hz and (c) 200 Hz frequency in 1 M NaNO<sub>3</sub> and one pretreatment before erosion.

**Figure S4a-S4c** provide the collected diffraction patterns of the Pd/C catalysts manufactured with 200 Hz, 100 Hz, and 20 Hz, respectively. In line with the previously investigated catalysts, the XRD patterns reveal the presence of two Pd phases attributed to strained and non-strained Pd for the Pd/C catalysts. The lattice parameter of the strained Pd NPs corresponds to approximately  $0.39950 \pm 0.00010$  nm,  $0.40107 \pm 0.00006$  nm, and  $0.40025 \pm 0.00006$  nm for an applied frequency of 200 Hz, 100 Hz, and 20 Hz, respectively. Assuming the strain arises from hydride formation, the H:Pd ratios reach  $\sim 0.43$ ,  $\sim 0.49$ , and  $\sim 0.46$ , respectively.<sup>[57]</sup> Similar to the previously investigated catalyst, we explored the weight ratio differences of the strained and non-strained Pd phases for the catalysts synthesized with different applied frequencies. Furthermore, independently of the strain presence, the frequency does not affect the crystallite size of the Pd NPs. An overview of all parameters extracted from XRD experiments can be found in **Table S1, and S2**.

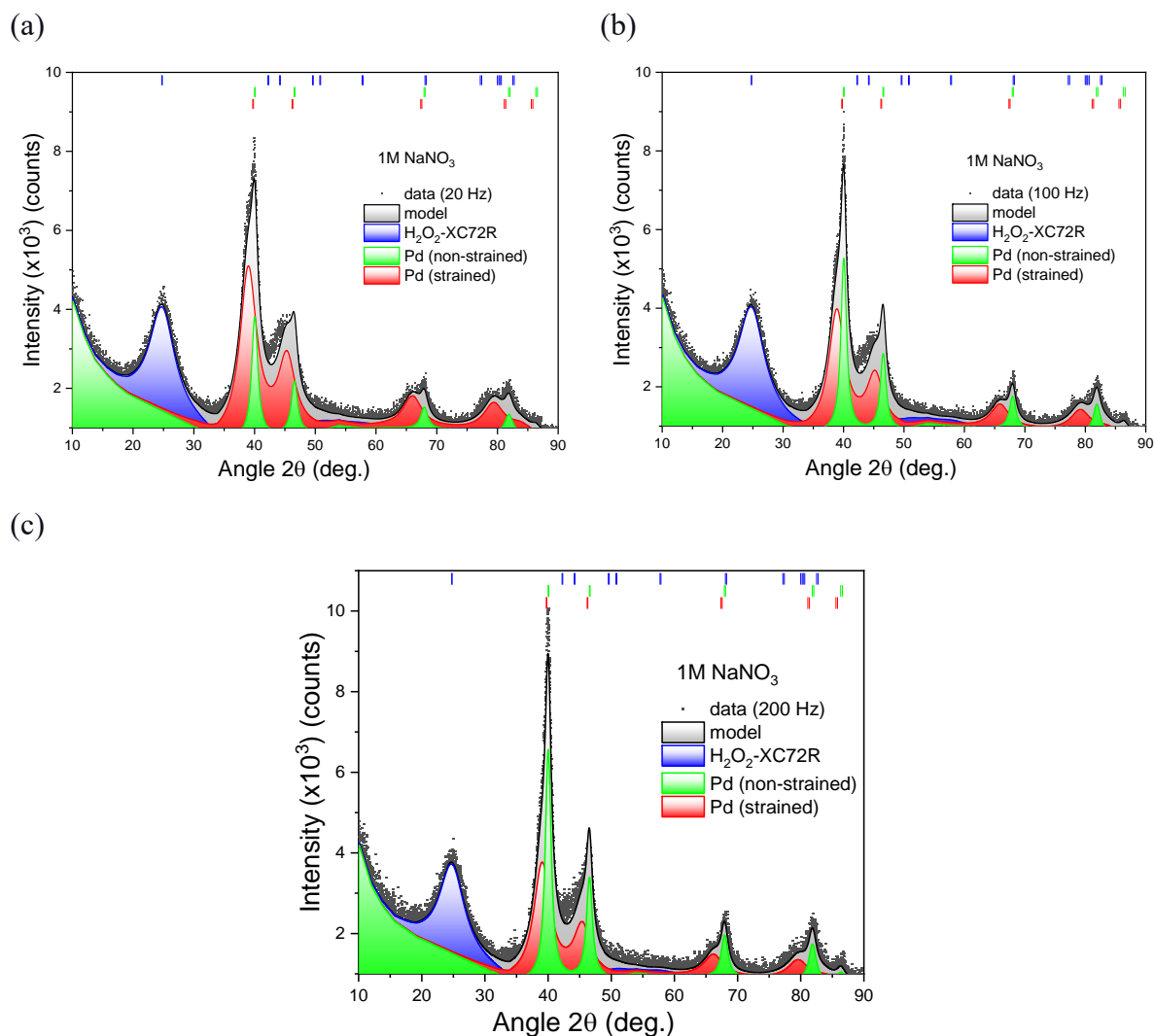


**Figure S4.** XRD patterns of the Pd/C catalyst synthesized with different applied frequencies in 1 M NaNO<sub>3</sub> with one pretreatment before erosion.

**Figure S5a-S5d** display the cyclic voltammograms recorded in Ar-saturated 0.1 M HClO<sub>4</sub> for the Pd/C catalysts produced with 200 Hz, 100 Hz, and 20 Hz frequencies, respectively. The small mass loading dissimilarities make the use of geometrical current densities reasonable to compare the size of characteristic Pd peaks. Those negligibly vary for a 2-fold frequency decrease from 200 Hz to 100 Hz but significantly change for the 10-fold frequency modification from 200 Hz to 20 Hz, as shown in Figure S5a. A similar trend arises for the specific surface areas (SSA), which continuously improves with a decrease in applied frequency. The lowest SSA of  $36.4 \pm 0.7 \text{ m}^2 \text{ g}_{\text{Pd}}^{-1}$  corresponds to the Pd/C catalysts synthesized with 200 Hz frequency. Accordingly, the SSA increases to  $40.8 \pm 2.3 \text{ m}^2 \text{ g}_{\text{Pd}}^{-1}$  and  $46.5 \pm 4.9 \text{ m}^2 \text{ g}_{\text{Pd}}^{-1}$  for the catalysts produced with a 100 Hz and 20 Hz frequency, respectively. For further analysis of the HER activities, Figure S5b illustrates the recorded HER polarization curves for the Pd/C

catalysts. The geometric activity (*GA*) evaluated at -5 mV vs. RHE increases with decreasing applied frequency, starting with  $0.72\pm 0.10 \text{ mA cm}_{\text{geo}}^{-2}$ ,  $0.75\pm 0.04 \text{ mA cm}_{\text{geo}}^{-2}$  and finally reaching  $0.80\pm 0.21 \text{ mA cm}_{\text{geo}}^{-2}$  for the Pd/C catalysts prepared with 200 Hz, 100 Hz, and 20 Hz frequencies, respectively. Furthermore, we combine the tendencies of the *MA* and *SA* with the applied frequency during electrochemical erosion. Figure S5c depicts the dependence of the *SA* on the applied frequency. The *SA* of the Pd NPs synthesized with 200 Hz, 100 Hz, and 20 Hz frequency corresponds to  $0.13\pm 0.02 \text{ mA cm}_{\text{Pd}}^{-2}$ ,  $0.14\pm 0.01 \text{ mA cm}_{\text{Pd}}^{-2}$ , and  $0.14\pm 0.04 \text{ mA cm}_{\text{Pd}}^{-2}$ , respectively. Under consideration of the error bars, the *SA* is unaffected by frequency changes during synthesis. Figure S5d relates the *MA* to the applied frequency during electrochemical erosion. The *MA*s evaluated at -5 mV vs. RHE increases with decreasing applied frequency. For the Pd/C catalysts produced with 200 Hz, 100 Hz, and 20 Hz frequency, the *MA* corresponds to  $48.2\pm 7.0 \text{ mA mg}_{\text{Pd}}^{-1}$ ,  $56.3\pm 3.3 \text{ mA mg}_{\text{Pd}}^{-1}$  and  $66.3\pm 17.5 \text{ mA mg}_{\text{Pd}}^{-1}$ , respectively. It is well known that the concave and convex surface geometry resulting from the shape and defect states influence the catalytic activity for surface-sensitive reactions like the HER<sup>[58,59,60]</sup> or ORR.<sup>[61,62,63,64]</sup> Theoretical concepts correlate the adsorption energy of the reaction intermediate with the so-called coordination (*CN*)<sup>[65,66,67]</sup> or "generalized" coordination number ( $\overline{CN}$ )<sup>[68]</sup> of the catalyst atoms. Since Pd strongly binds the adsorbed hydrogen intermediate, it limits the HER activity through inhibited desorption of the gaseous H<sub>2</sub> molecules.<sup>[69]</sup> Therefore, HER activity is likely to be enhanced at atoms with slightly higher coordination numbers, which exist at cavity-like surface defects. This theoretical postulation matches the results of the Pd/C catalyst synthesized with 200 Hz, 100 Hz, and 20 Hz frequency. The defect density of the Pd NP significantly increases with a smaller frequency, as shown in the inset of Figure S2d, which displays a single Pd NP with a resolution scale bar of 5 nm. The blue dashed line indicates the "cloudy" shape of the NP, with arrows pointing toward concave-like defects. Those concavities of the 20 Hz Pd NP sample lead to the increased *MA* compared to the Pd NP with sharp edges formed by applying 200 Hz, as illustrated in Figure S5d.

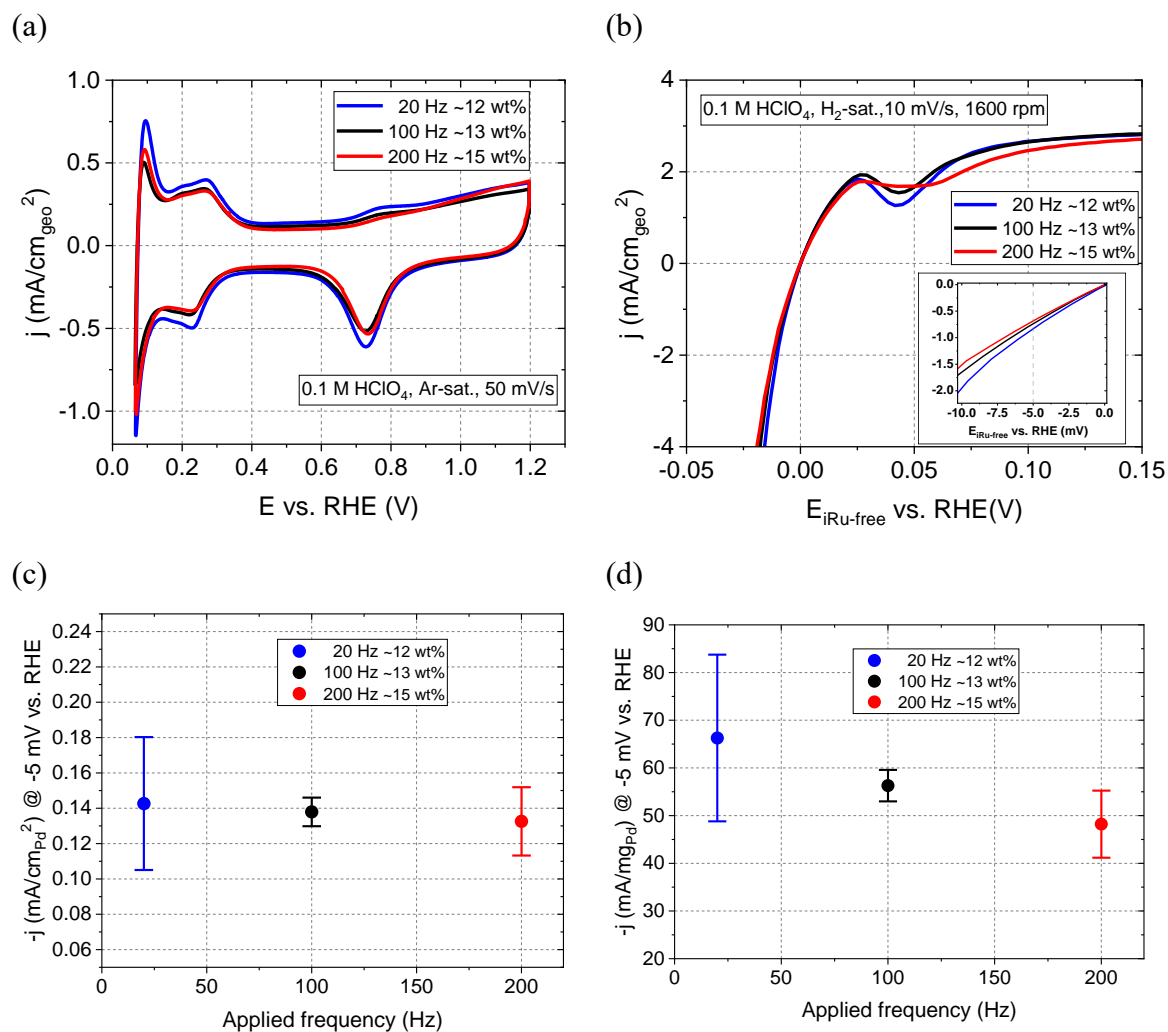


**Figure S5.** (a) CVs of Pd/C catalysts synthesized with 200 Hz, 100 Hz, and 20 Hz frequency. The curves were recorded in Ar-saturated 0.1 M HClO<sub>4</sub> at a scan rate of 50 mV s<sup>-1</sup> and rotation speed of 400 rpm. (b) Characteristic *i*R<sub>U</sub>-corrected HER polarization curves (cathodic scan) of Pd/C catalysts synthesized with 200 Hz, 100 Hz, and 20 Hz frequency. The curves were recorded in H<sub>2</sub>-saturated 0.1 M HClO<sub>4</sub> at a scan rate of 10 mV s<sup>-1</sup> and a rotation speed of 1600 rpm. Comparison of the (c) SA (d) MA evaluated at -5 mV vs. RHE with the applied frequency during electrochemical erosion.

**Table S1.** Lattice parameter of the strained and non-strained Pd phases and their refined weight fractions in the total Pd/C catalyst batch.

Pd/C batch	Lattice parameter	Lattice parameter	Weight ratio
	(phase 1; strained Pd) [nm]	(phase 2; non-strained Pd) [nm]	(phase 1: phase 2) [wt%]
Pd/C 1 M NaNO <sub>3</sub>	0.39285±0.00008	0.39008±0.00002	63:37
Pd/C 2 M NaNO <sub>3</sub>	0.39224±0.00010	0.39044±0.00002	48:52
Pd/C 4 M NaNO <sub>3</sub>	0.39309±0.00012	0.39082±0.00003	53:47
Pd/C 20 Hz	0.40025±0.00006	0.39012±0.00003	79:21
Pd/C 100 Hz	0.40107±0.00006	0.39005±0.00002	66:34
Pd/C 200 Hz	0.39950±0.00010	0.39021±0.00002	59:41

**Table S2.** Average crystallite size of the strained and non-strained Pd phases and the H<sub>2</sub>O<sub>2</sub>-XC72R Vulcan Carbon as obtained from XRD profiles.

Pd/C batch	Average crystallite size	Average crystallite size	Average crystallite size
	(phase 1; strained Pd) [nm]	(phase 2; non-strained Pd) [nm]	(H <sub>2</sub> O <sub>2</sub> -XC72R) [nm]
Pd/C 1 M NaNO <sub>3</sub>	1.9	6.1	1.3
Pd/C 2 M NaNO <sub>3</sub>	1.8	4.8	1.4
Pd/C 4 M NaNO <sub>3</sub>	1.8	5.2	1.2
Pd/C 20 Hz	1.8	5.3	1.2
Pd/C 100 Hz	1.9	5.8	1.2
Pd/C 200 Hz	1.9	5.8	1.2

**TGA analysis of Pd/C catalysts synthesized in 1 M, 2 M and 4 M NaNO<sub>3</sub>**

**Figure S6** presents the TGA results obtained for the Pd/C catalysts synthesized in 1 M, 2 M and 4 M NaNO<sub>3</sub>. A detailed description of the TGA measurement procedure can be found in the experimental section of the main manuscript.

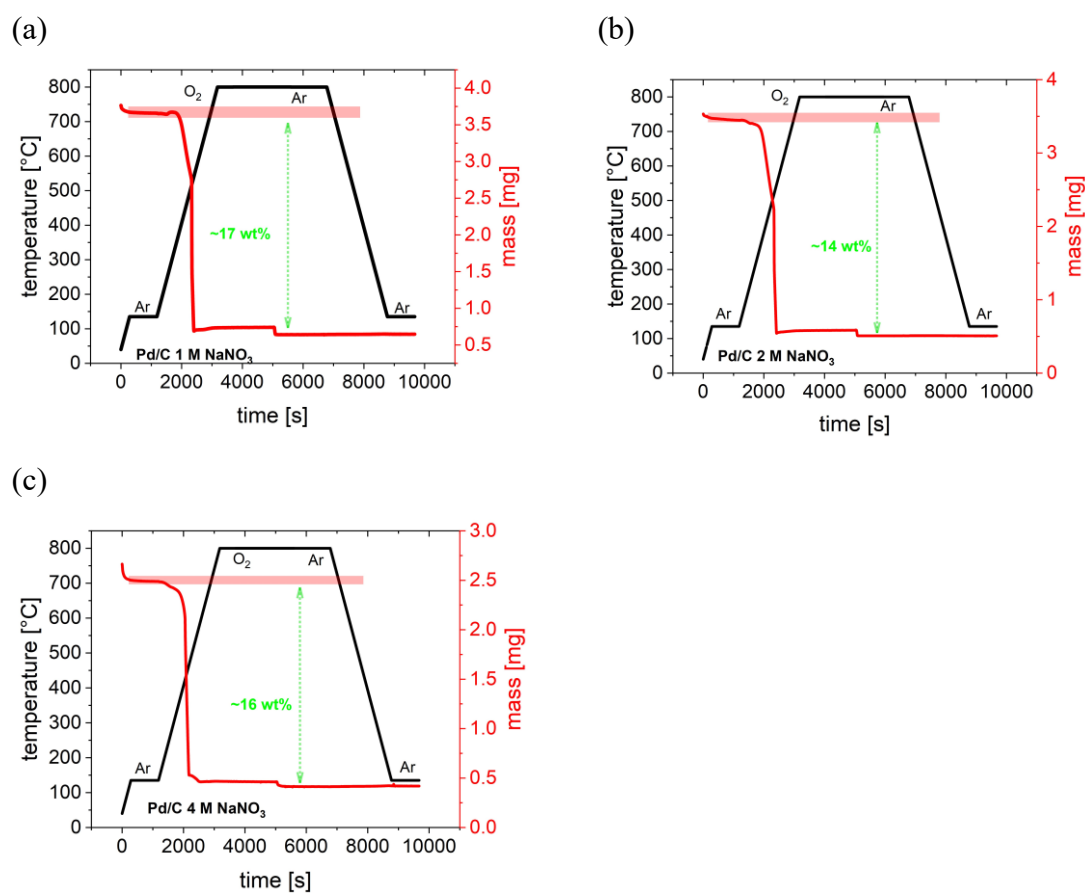


**Figure S6.** TGA measurements of the Pd/C catalysts synthesized in (a) 1 M, (b) 2 M, and (c) 4 M NaNO<sub>3</sub>. The approximated weight loading was determined using the evaluation procedure from the STARE Software (V 16.30) from Mettler-Toledo.

- 
- [1] J. E. Erchinger, M. van Gemmeren, *Asian J. Org. Chem.* **2020**, *10*, 50.
- [2] A. Winiwarter, L. Silvioli, S. B. Scott, K. Enemark-Rasmussen, M. Saric, D. B. Trimarco, P. C. K. Vesborg, P. G. Moses, I. E. L. Stephens, B. Seger, J. Rossmeisl, I. Chorkendorff, *Energy Environ. Sci.* **2019**, *12*, 1055.
- [3] S. R. Kim, E. C. Wegener, M. C. Yang, M. E. O'Reilly, S. Oh, C. H. Hendon, J. T. Miller, Y. Surendranath, *J. Am. Chem. Soc.* **2020**, *142*, 20631.
- [4] Q. Chang, P. Zhang, A. H. B. Mostaghimi, X. Zhao, S. R. Denny, J. H. Lee, H. Gao, Y. Zhang, H. L. Xin, S. Siahrostamin, J. G. Chen, Z. Chen, *Nat. Commun.* **2020**, *11*, 2178.
- [5] H. Meng, D. Zeng, F. Xie, *Catalysts* **2015**, *5*, 1221.
- [6] N. Shaari, S. K. Kamarudin, R. Bahru, S. H. Osman, N. A. I. M. Ishak, *Int. J. Energy Res.* **2021**, *45*, 6644.
- [7] L. Huang, J. Zou, J. Ye, Z.-Y. Zhou, Z. Lin, X. Kang, P. K. Jain, S. Chen, *Angew. Chem., Int. Ed.* **2019**, *58*, 8794.
- [8] A. Ali, P. K. Shen, *J. Mater. Chem. A* **2019**, *7*, 22189.
- [9] S. Lee, H. Cho, H. J. Kim, J. W. Hong, Y. W. Lee, *Materials* **2021**, *14*, 2970.
- [10] M. Jin, H. Zhang, Z. Xie, Y. Xia, *Energy Environ. Sci.* **2012**, *5*, 6352.
- [11] M. Shao, *J. Power Sources* **2011**, *196*, 2433.
- [12] M. Ma, W. Zhu, Q. Shao, H. Shi, F. Liao, C. Shao, M. Shao, *ACS Appl. Nano Mater.* **2021**, *4*, 1478.
- [13] T. Wang, A. Chutia, D. J. L. Brett, P. R. Shearing, G. He, G. Chai, I. P. Parkin, *Energy Environ. Sci.* **2021**, *14*, 2639.
- [14] O. Piermatti, *Catalysts* **2021**, *11*, 1258.
- [15] J. Y. Park, C. Aliaga, J. R. Renzas, H. Lee, G. A. Somorjai, *Catal. Lett.* **2009**, *129*, 1.
- [16] S. Brimaud, C. Coutanceau, E. Garnier, J.-M. Léger, F. Gérard, S. Pronier, M. Leoni, *J. Electroanal. Chem.* **2007**, *602*, 226.
- [17] T. J. P. Hersbach, M. T. M. Koper, *Curr. Opin. Electrochem.* **2021**, *26*, 100653.
- [18] J. Feng, D. Chen, A. S. Sediq, S. Romeijn, F. D. Tichelar, W. Jiskoot, J. Yang, M. T. M. Koper, *ACS Appl. Mater. Interfaces* **2018**, *10*, 9532.
- [19] S. Sui, X. Wang, X. Zhou, Y. Su, S. Riffat, C. Liu, *J. Mater. Chem.* **2016**, *5*, 1808.
- [20] S. Pérez-Rodríguez, E. Pastor, M. J. Lázaro, *Int. J. Hydrogen Energy* **2018**, *43*, 7911.
- [21] X. Chen, S. Chen, W. Huang, J. Zheng, Z. Li, *Electrochim. Acta* **2009**, *54*, 7370.

- [22] W. Huang, L. Fu, Y. Yang, S. Hu, C. Li, Z. Li, *Electrochem. Solid-State Lett.* **2010**, *13*, K46.
- [23] W. Huang, S. Chen, J. Zheng, Z. Li, *Electrochem. Commun.* **2008**, *11*, 469.
- [24] J. Liu, W. Huang, S. Chen, S. Hu, F. Liu, Z. Li, *Int. J. Electrochem. Sci.* **2009**, *4*, 1302.
- [25] A. I. Yanson, P. Rodriguez, N. Garcia-Araez, R. V. Mom, F. D. Tichelar, M. T. M. Koper, *Angew. Chem. Int. Ed.* **2011**, *50*, 6346.
- [26] T. J. P. Hersbach, I. T. McCrum, D. Anastasiadou, R. Wever, F. Calle-Vallejo, M. T. M. Koper, *ACS Appl. Mater. Interfaces* **2018**, *10*, 39363.
- [27] A. I. Yanson, P. V. Antonov, P. Rodriguez, M. T. M. Koper, *Electrochim. Acta* **2013**, *112*, 913.
- [28] P. Rodriguez, F. D. Tichelar, M. T. M. Koper, A. I. Yanson, *J. Am. Chem. Soc.* **2011**, *133*, 17626.
- [29] J. Fichtner, B. Garlyyev, S. Watzele, H. A. El-Sayed, J. N. Schwämmlein, W. Li, F. M. Maillard, L. Dubau, J. Michalicka, J. M. Macak, A. Holleitner, A. S. Bandarenka, *ACS Appl. Mater. Interfaces* **2019**, *11*, 5129.
- [30] B. Garlyyev, S. Watzele, J. Fichtner, J. Michalická, A. Schökel, A. Senyshyn, A. Perego, D. Pan, H. A. El-Sayed, J. M. Macak, P. Atanassov, I. V. Zenyuk, A. S. Bandarenka, *Nano Res.* **2021**, *14*, 2762.
- [31] J. Fichtner, S. Watzele, B. Garlyyev, R. M. Kluge, R. M. Haimerl, H. A. El-Sayed, W. Li, F. M. Maillard, L. Dubau, R. Chattot, J. Michalicka, J. M. Macak, W. Wang, D. Wang, T. Gigl, C. Hugenschmidt, A. S. Bandarenka, *ACS Catal.* **2020**, *10*, 3131.
- [32] S. Sarkar, S. C. Peter, *Inorg. Chem. Front.* **2018**, *5*, 2060.
- [33] M. R. Louthan Jr., *J. Fail. Anal. Prev.* **2008**, *8*, 289.
- [34] A. Barnoush, H. Vehoff, *Acta Mater.* **2010**, *58*, 5274.
- [35] Y. Murakami, T. Kanazaki, Y. Mine, *Metall. Mater. Trans. A* **2010**, *41*, 2548.
- [36] Gilbert Bellanger, Corrosion Cracking in Palladium. Scholarly Community Encyclopedia. <https://encyclopedia.pub/entry/4>, accessed: August, 2022).
- [37] T. O. Schmidt, A. Ngoipala, R. L. Arevalo, S. A. Watzele, R. Lipin, R. M. Kluge, S. Hou, R. W. Haid, A. Senyshyn, E. L. Gubanova, A. S. Bandarenka, *Small* **2022**, *18*, 2202410.
- [38] J. M. Sobral, T. W. Clyne, R. Rezk, A. E. Markaki, *Surf. Coat. Technol.* **2017**, *326*, 327.
- [39] L. C. Yule, E. Daviddi, G. West, C. L. Bentley, P. R. Unwin, *J. Electroanal. Chem.* **2020**, *872*, 114047.

- [40] S. Khodabakhshi, P. F. Fulvio, E. Andreoli, *Carbon* **2020**, *162*, 604.
- [41] Z. Zhao, M. M. Flores Espinoza, J. Zhou, W. Xue, X. Duan, J. Miao, Y. Huang, *Nano Res.* **2019**, *12*, 1467.
- [42] J. D. Benck, A. Jackson, D. Young, D. Rettenwander, Y. Chiang, *Chem. Mater.* **2019**, *31*, 4234.
- [43] Z. Zhao, M. M. Flores Espinoza, J. Zhou, W. Xue, X. Duan, J. Miao, Y. Huang, *Nano Res.* **2019**, *12*, 1467, (Supplementary Material).
- [44] C. F. Holder, R. E. Schaak, *ACS Nano* **2019**, *13*, 7359.
- [45] X. Qin, L. Zhang, G.-L. Xu, S. Zhu, Q. Wang, M. Gu, X. Zhang, C. Sun, P. B. Balbuena, K. Amine, M. Shao, *ACS Catal.* **2019**, *9*, 9614.
- [46] FUELCELL Store, 20% Palladium on Vulcan.  
[https://www.fuelcellstore.com/product/product&product\\_id=666](https://www.fuelcellstore.com/product/product&product_id=666), accessed: December, 2022).
- [47] M. Smiljanić, M. Bele, L. Moriau, F. Ruiz-Zepeda, M. Šala, N. Hodnik, *J. Phys. Chem. C* **2021**, *125*, 27534.
- [48] J. Rodríguez-Carvajal, *Phys. B* **1993**, *192*, 55.
- [49] G. Cliff, G. W. Lorimer, *J. Microsc.* **1975**, *103*, 203.
- [50] C. A. Schneider, W. S. Rasband, K. W. Eliceiri, *Nat. Methods* **2012**, *9*, 671.
- [51] J. Lee, J. H. Bang, *ACS Energy Lett.*, **2020**, *5*, 2706.
- [52] L. Fang, Q. Tao, M. Li, L. Liao, D. Chen, Y. Chen, *Chin. J. Chem. Phys.* **2010**, *23*, 543.
- [53] S. Henning, J. Herranz, H. A. Gasteiger, *J. Electrochem. Soc.* **2014**, *162*, F178.
- [54] M. Hara, U. Linke, T. Wandlowski, *Electrochim. Acta* **2007**, *52*, 5733.
- [55] M. Wang, X. Qin, K. Jiang, Y. Dong, M. Shao, W. Cai, *J. Phys. Chem. C* **2017**, *121*, 3416.
- [56] T. J. P. Hersbach, M. T. M. Koper, *Curr. Opin. Electrochem.* **2021**, *26*, 100653.
- [57] Z. Zhao, M. M. Flores Espinoza, J. Zhou, W. Xue, X. Duan, J. Miao, Y. Huang, *Nano Res.* **2019**, *12*, 1467, (Supplementary Material).
- [58] Y. Lian, C. Csoklich, D. McLaughlin, O. Schneider, A. S. Bandarenka, *ACS Appl. Mater. Interfaces* **2019**, *11*, 12476.
- [59] E. Mitterreiter, Y. Liang, M. Golibrzuch, D. McLaughlin, C. Csoklich, J. D. Bartl, A. Holleitner, U. Wurstbauer, A. S. Bandarenka, *npj 2D Mater. Appl.* **2019**, *3*.
- [60] R. M. Kluge, R. W. Haid, I. E. L. Stephens, F. Calle-Vallejo, A. S. Bandarenka, *Phys. Chem. Chem. Phys.* **2021**, *23*, 10051.

- 
- [61] F. Calle-Vallejo, M. D. Pohl, D. Reinisch, D. Loffreda, P. Sautet, A. S. Bandarenka, *Chem. Sci.* **2016**, *8*, 2283.
- [62] Y. Liang, D. McLaughlin, C. Csoklich, O. Schneider, A. S. Bandarenka, *Energy Environ. Sci.* **2019**, *12*, 351.
- [63] R. M. Kluge, E. Psaltis, R. W. Haid, S. Hou, T. O. Schmidt, O. Schneider, B. Garlyyev, F. Calle-Vallejo, A. S. Bandarenka, *ACS Appl. Mater. Interfaces* **2022**, *14*, 19604.
- [64] R. M. Kluge, R. W. Haid, A. Riss, Y. Bao, K. Seufert, T. O. Schmidt, S. A. Watzele, J. V. Barth, F. Allegretti, W. Auwärter, F. Calle-Vallejo, A. S. Bandarenka, *Energy Environ. Sci.* **2022**, *15*, 5181.
- [65] F. Calle-Vallejo, M. T. M. Koper, *ACS Catal.* **2017**, *7*, 7346.
- [66] H. Li, Y. Li, M. T. M. Koper, F. Calle-Vallejo, *J. Am. Chem. Soc.* **2014**, *136*, 15694.
- [67] F. Calle-Vallejo, D. Loffreda, M. T. M. Koper, P. Sautet, *Nat. Chem.* **2015**, *7*, 403.
- [68] F. Calle-Vallejo, J. Tymoczko, V. Colic, Q. H. Vu, M. D. Pohl, K. Morgenstern, D. Loffreda, P. Sautet, W. Schuhmann, A. S. Bandarenka, *Science* **2015**, *350*, 185.
- [69] J. K. Nørskov, T. Bligaard, A. Logadottir, J. R. Kitchin, J. G. Chen, S. Pandelov, U. Stimming, *J. Electrochem. Soc.* **2005**, *152*.